Utrecht University

Master Thesis

Thermodynamics of Topological Kondo Insulators

Author:
Jette van den Broeke

Supervisor:
Prof. dr. Cristiane de Morais Smith
and
Sander Kempkes MSc

Institute for Theoretical Physics
Department of Physics and Astronomy

June 2017

Abstract

We investigate the thermodynamic behavior of topological Kondo insulators using a mean-field slave boson approximation and Hill thermodynamics. In particular, we focus on SmB_6 and consider the order of the topological Kondo insulator to band insulator phase transition, and the bulk and boundary contribution of the system to the heat capacity. We find that the order of the phase transition can be accurately predicted using the critical exponents of the system, and is consistent with the Josephson hyperscaling relation. Furthermore, we find that the anomalous heat capacity of SmB_6 is probably not explained by edge states in the mean-field model.

Acknowledgements

I would first like to thank my thesis supervisor Prof. dr. Cristiane de Morais Smith. She was always willing to help whenever I had a problem with my research. She consistently allowed me to do my own research, but enthusiastically steered me in the right direction whenever she thought I needed it. I would also like to thank my daily supervisor Sander Kempkes MSc, for his active participation and input. I would further like to thank Anton Quelle MSc., for fruitful discussions and making his computer available for calculations, Snader Kooi MSc., for running a lot of calculations on his computer, and Peter Cats, for useful discussions bringing us both to a better understanding of the material.

Finally, I would like to explicitly thank my family, my friends, and my girlfriend for supporting and continuously encouraging me throughout my years of study and through the process of researching and writing this thesis. This accomplishment would not have been possible without them. Thank you.

Public Summary

In this thesis, we investigate the properties of samarium hexaboride (SmB_6). SmB_6 is the first experimentally measured Kondo insulator. This means that due to the effects of interaction between electrons, it is insulating at low temperatures and conducting at high temperatures. In order to explain behavior of SmB_6 that was long not understood, it has recently been proposed that SmB_6 is not only a Kondo insulator, but is also topological. This would mean that the material at low temperature, although insulating in the bulk, would have conducting states on the surface. This is interesting as topological materials are hoped to be a solution to current problems in the physical realization of quantum computing devices, and there is currently no known material which is a three-dimensional topological insulator with a fully gaped bulk.

We model SmB_6 using mean-field theory: we approximate the interactions between electrons as a background field, resulting in an effective non interacting theory. We then investigate when the edge states appear in this model as we vary the temperature and an important parameter of the system, the hybridization, which characterizes the strength of the interaction between two kind of electrons in the model. This results in a phase diagram separating the phases where the model is metallic, insulating in the bulk with metallic surface states, and completely insulating.

In order to calculate the heat capacity of the system, and investigate the transition between different phases, we then need thermodynamics. Thermodynamics is the formalism linking the microscopic properties of a system, such as the location of each particle in te system, to macroscopic properties such as energy and temperature, using statistical methods. Unfortunately, in most thermodynamic identities, the thermodynamic limit is considered. In this limit, there are so many particles that the boundaries of the system are no longer relevant. However, in the case of topological insulators, we are interested in exactly these boundaries, as the edge states appear there. We therefore use a trick named Hill thermodynamics to obtain the boundary contributions to the thermodynamics separately from the bulk ones.

Applying the Hill thermodynamics, we find the model we used can probably not explain the experimentally obtained heat capacity, implying that the heat capacity is not governed by surface effects. We furthermore find that the order of the phase transition from insulating state with conducting edges to completely insulating, has interesting behavior that does not seem to match previous results. This order is determined by calculating which order of the derivative of the free energy with respect to the parameter driving the phase transition is discontinuous. We found that both the orders in our model as the orders found in previous results can be accurately predicted by the critical exponents of the system. This is convenient, as critical exponents are generally easy to calculate.

Contents

Introduction

Topological insulators are materials that are insulating in the bulk, but have conducting edge states at the boundaries. These edge states are protected against small impurities, since they are protected by the symmetries of the bulk Hamiltonian. This makes the edge states of a topological insulator ideal candidates for quantum computing components, where robustness of the quantum states are important. The topic of topological insulators is relatively new, however, a lot of progress has been made on the subject in the last decade. Following the rapid developments in the field, last years Nobel prize in physics was awarded with one half to David J. Thouless, and the other half to F. Duncan M. Haldane and J. Michael Kosterlitz, "for theoretical discoveries of topological phase transitions and topological phases of matter". Although the first three-dimensional topological insulator, bismuth antimonide, has been measured [1], no truly bulk gapped three-dimensional topological insulator has been found. This makes the currently known three-dimensional topological insulators less suitable for potential use in next generation electronic devices. Therefore, the search for a three dimensional topological insulator with a fully gapped bulk continues [2].

One of the most promising realizations of a three-dimensional topological insulator with a fully gapped bulk is samarium hexaboride (SmB_6). SmB_6 is a Kondo insulator, meaning that below a certain temperature, the Kondo temperature, the otherwise metallic system becomes insulating. This transition is caused by a hybridization between conducting d-electrons and localized f-electrons at low temperature, opening up a hybridization gap. SmB_6 is the first known Kondo insulator [3], and was discovered almost 50 years ago. However, it has long had unexplained behavior. The most important of which, is that although a gap opens up at low temperature, the resistivity does not go to infinity as the temperature goes to zero. Instead, there is a residual conductivity. This experimental feature was first explained by the presence of impurities in the samples but the effect did not decrease with improving sample quality [4]. In light of the recent developments on the field of topological insulators, Dzero et al. [5] proposed that the Kondo insulator could be topological, and the edge states could be responsible for the residual conductivity. Although there is still experimental controversy about whether or not SmB_6 actually is a topological insulator, SmB_6 remains a strong candidate to be the first three-dimensional topological insulator with a truly insulating bulk [6].

Besides the residual conductivity, there is an other unexplained feature of SmB_6. Although SmB_6 is an insulator for low temperatures, the low temperature heat capacity is reminiscent to that of a metal, as shown in figure 1.1 [7, 8]. It might seem logical to

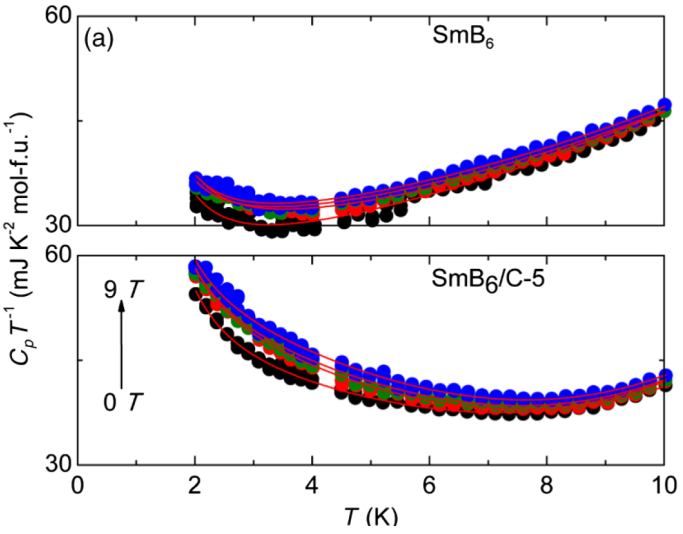

FIGURE 1.1: Experimentally measured heat capacity of SmB_6. Here the black dots in the upper graph indicate the measurements on undoped SmB_6 with zero magnetic field. Figure source: [7].

look for an explanation for this phenomenon in the direction of the topological nature of the system. Indeed, it was shown by Kempkes et al. [9], using thermodynamics of finite-size systems, that surface states can have a significant contribution to the heat capacity. However, Knolle et al. proposed in reference [10], that the behavior of the heat capacity cannot be explained by the presence of edge modes, but instead results from the interacting nature of the system. Therefore, a mean-field model should not be able to explain the heat capacity. We will investigate this problem using an approach not tried so far: apply Hill thermodynamics as in reference [9] on a mean field SmB_6 model, to see if the edge states can be responsible for the unexpected behavior of the heat capacity in SmB_6.

The thermodynamics used in reference [9] enables us to also investigate an other interesting feature of topological insulators, namely the phase transition from a topological phase to a trivial phase, and the order of this transition. In reference [9] it is shown that the five most common models for topological insulators obey an universality law [9]. Although the phase diagram of Kondo insulators has been studied previously [11–13], using different mean-field approaches, the orders of the phase transitions have not been considered. It is therefore interesting to see whether the universality rule for the order of the phase transition also applies to Kondo insulators, and in particular for SmB_6 models. This is especially interesting since SmB_6 has a much more complicated band structure an richer phase diagram then the models studied in reference [9].

Hill thermodynamics is a formalism that makes it possible to calculate bulk and boundary contributions to thermodynamic quantities [14]. This is different from the general

thermodynamic approach, in which the thermodynamic limit is applied and the boundaries of the system are neglected. Leaving out the boundary is not desirable in this case however, since we are particularly interested in exactly the influence of these boundaries. Therefore, it is necessary to explicitly consider thermodynamics of finite systems, for which the Hill approach is excellently suited.

There are various models that describe Kondo insulators in general and/or SmB_6 in particular. The simplest model by Dzero et al. [15] only uses 4 bands, a spin up and down d-electron, and a spin up and down f-electron. However, this model does not accurately describe the way the bandgap closes, since in case of SmB_6, more bands are present. Therefore, we use the model proposed by Baruselli et al. [16], who use a 10 band model, with parameters obtained from a DFT calculation, and determine the most important contributions following from an up to seventh nearest neighbor approach. An additional upside of this model is that it is less likely to predict phases that do not actually exist, as it was shown by Dzero [11], that the presence of a weak topological insulating phase was dependent of the amount of bands taken into account.

In this thesis, we show that the order of the topological phase transition in bulk and boundary for the model by Baruselli et al. [16] of SmB_6 does not obey the universality rule found in reference [9]. We find that the order of the phase transition can be understood by considering critical exponents. In this description, we indeed recover the law discovered by Kempkes et al. for the systems that were investigated in this reference. The difference between these models and the model investigated in this thesis is explained by different values of critical exponents. Furthermore, we show that the anomalous heat capacity of SmB_6 is probably not caused by the presence of the edge states, which is in line with the proposal by Knolle et al. [10].

We will continue this thesis in chapter 2 with an overview of different kinds of materials and from there introduce the concept of a topological insulator. Then, we will see several examples of topological systems, and finally focus on time-reversal invariant topological insulators, to which Kondo insulators belong, and discuss topological Kondo insulators in general and SmB_6 in particular. Next, in chapter 3 we will discuss thermodynamics of finite-size systems, the role of Hill thermodynamics, and how it can be applied on a specific model. In chapter 4 we will discuss what critical exponents are, and how they can predict the order of the phase transition. Then, in chapter 5, we will present our results and finally in chapter 6 we will discuss these results and the following conclusions.

Topological Insulators

In this thesis, we investigate topological Kondo insulators, and provide a thermodynamic description of their topological behavior. However, before we look further into the properties of the topological Kondo insulator, it is useful to first review the types of insulators, and the main properties of topological materials.

2.1 Different Types of Insulators

The most basic classification of materials is based on their transport properties, which is strongly dependent on their band structure. Using Bloch's theorem, we can evaluate single-electron states, and determine the dependence of the energy of these states on the momentum. If the resulting band structure is not gapped around the Fermi energy, the material is classified as a metal. In this case, electrons can continuously move to a higher energy level when an electric field is applied, and thus the material is conducting. If, on the other hand, there is a gap around the Fermi energy, the electrons have to make an energy jump in order to reach a higher energy level. When the gap is large enough, the material becomes insulating, and is called a band insulator. When the gap is small, there can still be some conductance in the material, making it a semi-conductor. This classification of metals semiconductors and insulators is depicted in figure 2.1. Unfortunately, this classification of materials is incomplete, as it only considers single-electron states in a periodic potential, it disregards important aspects like disorder, interactions, finite size effects, and the topology of the bands. Taking these aspects into account, we find a much wider range of insulators.

Firstly, let us consider the Anderson insulator. This type of insulator does not exhibit a gap, but is insulating due to disorder, which localizes the electron states [18]. Secondly, interaction between particles can lead to a Mott insulator. In a Mott insulator, the repulsion between electrons is much stronger than the hopping, which again leads the electrons to localize on different sites. Thirdly, in a so called Kondo insulator, the conduction electrons interact with local moments. If there are as many conduction electrons as there are local moments, every conduction electron can become bound, thus creating an insulator. Finally, there is a special class of materials which are known as topological insulators. A topological insulator is insulating in the bulk, but has metallic boundary states. Although the bulk of a topological insulator seems very similar to that of a band insulator, it is fundamentally different. The difference lies in the fact that

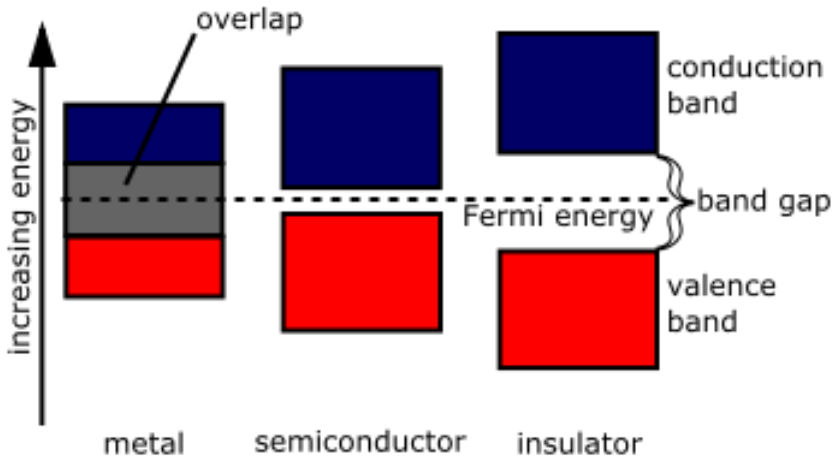

FIGURE 2.1: Basic classification of materials. If the band structure is not gapped around the Fermi energy, the material is classified as a metal. In this case, the material is conducting. If there is a small gap around the Fermi energy, the material is a semiconductor, and when the gap is large enough, the material becomes insulating. Image source: [17]

the bulk band structure of a topological insulator cannot be deformed into the band structure of a band insulator continuously, that is without closing the energy gap in the process. We therefore say that a topological insulator is topologically different from the band insulator, and is in a topological phase. Contrary to Landau's approach, in which phases are characterized in therms of broken underlying symmetries, the topological phase is defined by the existence of certain fundamental properties that are insensitive to smooth changes in the system's parameters. These fundamental properties can only change if the system passes through a quantum phase transition (a closing of the band gap, or a change of the symmetry class) [19]. A Kondo insulator becomes an insulator due to interactions, and can even exhibit a topological phase under certain circumstances.

Besides insulators, there also are conducting materials that do not fall into the standard band-structure classification. Superconductors have an energy gap, but can conduct electricity without resistance. This is caused by a phonon mediated net attractive interaction between electrons. Below the critical temperature T_c, it becomes energetically favorable for the system to form pairs of electrons instead of the Bloch single particle states. These pairs can then conduct electricity without resistance, since scattering them would mean breaking the pair, for which the electrons would have to cross an energy gap to the single-particle states [20]. Because superconductors have a band gap, just like band insulators, they may also exhibit a topological phase.

2.2 Topological Materials

In order to better understand the topological phase and the concepts associated with it, we will now describe several important examples of topological materials. We will start by considering the Kitaev chain, which is a model for a one-dimensional topological superconductor.

2.2.1 One-Dimensional Topological Superconductor: the Kitaev Chain

The Kitaev chain models a one-dimensional superconducting chain, in which each site is either empty or filled with a spinless fermion. Although the physical realization of the model is difficult for several reasons (one of them is that electrons, are not spinless), it can be done by inducing superconductivity to the material by using the proximity effect of a nearby superconductor. This method has been applied successfully to measure signatures of Majorana bound states [21], which are the predicted edge states of this system [22]. The model is especially useful, because the Kitaev chain has possible applications in quantum computing. It was originally proposed as a possible realization of quantum memory, since it offers a way to construct decoherence-protected degrees of freedom in quantum wires [22].

The Hamiltonian describing the Kitaev chain of length N is [22]

$$H = -\mu \sum_{n=1}^{N} \left(c_n^\dagger c_n - \frac{1}{2} \right) - t \sum_{n=1}^{N-1} (c_{n+1}^\dagger c_n + h.c.) + \Delta \sum_{n=1}^{N-1} (c_n c_{n+1} + h.c.). \tag{2.1}$$

Here, c_n is the annihilation operator for a spinless fermion at site n, μ is the chemical potential, t the hopping amplitude, and Δ the superconducting pairing amplitude. We can understand the term $\Delta \sum_n (c_n c_{n+1} + h.c.)$ as a mean field approximation of the attractive nearest-neighbor electron-electron interaction $\sum_n c_{n+1}^\dagger c_n^\dagger c_n c_{n+1}$.

To calculate the eigenenergies of the Kitaev chain, we need to diagonalize the Hamiltonian because the $\Delta \sum_n (c_n c_{n+1} + h.c.)$ term is off diagonal. It is easier, however to first double the degrees of freedom in the system by writing: $H = C^\dagger \mathcal{H} C$, where $C = (c_1, c_2, ...c_n, c_1^\dagger, c_2^\dagger, ..., c_n^\dagger)$, and then calculate the eigenvalues of $\mathcal{H}$. In this picture, $c_1^\dagger$ is both a creation operator of an electron and an annihilation operator of a hole. This symmetry is known as the particle-hole symmetry. The particle-hole symmetry implies that the energy spectrum of the Hamiltonian is symmetric around zero. Namely, if $\overrightarrow{u}$ is an eigenvector of $\mathcal{H}$, one can create an eigenstate with the operator $\overrightarrow{u} C^\dagger$, with corresponding energy E. Creating this state should have the same effect as annihilating the

particle hole reversed state defined by $\overrightarrow{u}^* C$. Thus, this state needs to have energy $-E$ and is also an eigenstate of the system.

We can also write the Hamiltonian in terms of Majorana operators γ_n. For this, we use the transformation:

$$\begin{aligned} c_n^\dagger &= \tfrac{1}{2}(\gamma_{2n-1} + i\gamma_{2n}), \\ c_n &= \tfrac{1}{2}(\gamma_{2n-1} - i\gamma_{2n}). \end{aligned} \tag{2.2}$$

Applying this transformation into equation (2.1), we find the Hamiltonian:

$$H = -\mu\frac{i}{2}\sum_{n=1}^{N}\gamma_{2n-1}\gamma_{2n} - \frac{i}{2}\sum_{n=1}^{N-1}\left[\gamma_{2n}\gamma_{2n+1}(t+\Delta) + \gamma_{2n-1}\gamma_{2n+2}(\Delta - t)\right]. \tag{2.3}$$

Using the inverse of the transformation, we find that $\gamma_n = \gamma_n^\dagger$. Thus, a Majorana mode cannot be empty or filled in the way fermion states are. We can also see that Majorana modes always come in pairs, a pair for each fermion. Because of this, it seems impossible to find a single isolated Majorana mode that is not close to its partner. However, it turns out that by tuning the parameters of the Hamiltonian, we can actually separate two Majoranas.

We start by considering two special cases for the Hamiltonian parameters. Firstly, there is the trivial case of isolated fermions $\Delta = t = 0$ and $\mu < 0$, in which the Hamiltonian becomes

$$H = -\mu\frac{i}{2}\sum_{n=1}^{N}\gamma_{2n-1}\gamma_{2n}. \tag{2.4}$$

In this case, the Majorana operators γ_{2n-1},γ_{2n} from the same electron are paired as depicted in the upper half of figure 2.2. The second case occurs for $\Delta = t > 0$, $\mu = 0$.

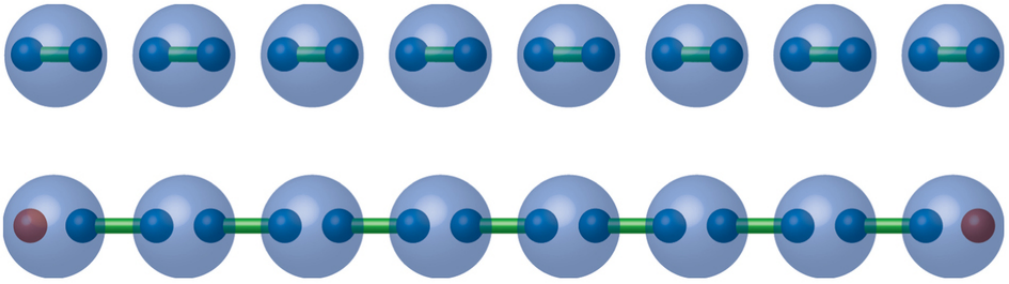

FIGURE 2.2: Two phases in the Kitaev chain. In the trivial phase (top), the Majorana modes (small blue spheres) of the same electron (big blue spheres) are paired together. In the topological phase (bottom), Majorana modes of adjacent electrons are paired together. Image source: [23].

In this case, the Hamiltonian becomes

$$H = -i\Delta \sum_{n=1}^{N-1} \gamma_{2n}\gamma_{2n+1}. \tag{2.5}$$

Now, the Majorana modes from different electrons are paired, as depicted in the lower half of figure 2.2, and the two end Majorana modes (γ_1 and γ_{2n}) are not paired. In fact, they do not appear in the Hamiltonian at all. Hence, there are two zero-energy states, localized at the ends of the chain. It turns out that these edge states are not exclusively there for this specific set of parameters. If we increase μ, the Majorana edge modes will persist until $\mu = \pm 2t$.

Are the two cases topologically equivalent or do they belong to different phases? In order to answer this question, we look at the bulk Hamiltonian. In this Hamiltonian, we eliminate the edges by imposing periodic boundary conditions and taking the limit of an infinite number of sites. Since now translational symmetry has been restored, we can Fourier transform the Hamiltonian to momentum space and calculate the band structure. This results in two energy bands, one with positive and one with negative energy,

$$E(k) = \pm\sqrt{(2t\cos k + \mu)^2 + 4\Delta^2 \sin^2 k}. \tag{2.6}$$

If we now again take $t = \Delta > 0$, we see that the energy gap closes exactly when $\mu = \pm 2t$. Thus, we have a quantum phase transition at this point, and we conclude that the two cases described above indeed belong to different phases. The phase transition occurs exactly when the Majorana edge modes disappear. We can understand this correspondence between the bulk and the edge (called the bulk-edge correspondence) in terms of symmetry.

Since the Hamiltonian is particle-hole symmetric, the energy spectrum has to be symmetric around zero energy. When $\mu = 0$, there are two zero-energy levels, corresponding to the two Majorana edge modes. These modes cannot move away from zero energy individually, since that would violate the particle-hole symmetry. Thus, we would have to couple the Majorana modes and move them away from zero energy simultaneously, in order to get rid of the zero-energy modes. This is, however, impossible, since they are localized far away from each other. The only way to move the modes away from zero energy is by closing the bulk energy gap, which is exactly what happens at the quantum phase transition.

Besides the appearance of the edge states at the closing of the energy gap, it also occurs that the topological invariants of the system can change. Although these invariants do not change when the Hamiltonian is varied smoothly, they can change when a phase

transition occurs. In the case of the Kitaev chain, a topological invariant can be defined using the Pfaffian; however, we will not do this here.

2.2.2 Two-Dimensional Chern Topological Insulators

As discussed in the previous section, we can define topological invariants that only change when the band gap closes. These topological invariants can be used to classify band structures. We say that structures that have the same value for a certain topological invariant are of the same class. One topologically invariant commonly used to classify two-dimensional band structures is the Chern number, a material with a non-trivial Chern number is called a Chern topological insulator.

The Chern number can best be understood by means of the Berry phase [24] that is associated with the Bloch wave functions $|u_m(k)\rangle$ of the system. If there are no degeneracies, $|u_m(k)\rangle$ picks up a well defined Berry phase when k is transported over a closed loop. This phase is given by the line integral over the loop of $A_m = i \langle u_m | \nabla_k | u_m \rangle$, which in turn is equal to the surface integral of the Berry flux $\nabla \times A_m$, over the area enclosed by the loop. We can define the Chern invariant as the integral of the Berry flux over the Brillouin zone,

$$n_m = \frac{1}{2\pi} \int d^2k \nabla \times A_m. \tag{2.7}$$

This yields us the total Chern number n, which is just the sum of the Chern invariants over all occupied bands, $n = \sum_{m=1}^{N} n_m$. It turns out that the Chern number is integer quantized. We can develop a physical intuition about this behavior by considering a simpler example. Instead of two-dimensional band structures, we now consider two-dimensional surfaces that are compact, edgeless and can be embedded in three dimensions, like a sphere and a torus, as depicted in figure 2.3. These surfaces can be topologically classified by the number of holes that they have, also called their genus. For example, a sphere has genus zero, and a torus has genus one. Besides counting the holes of the surface, the genus can also be calculated by integrating over the Gaussian curvature of the surface. The Chern number is very similar to the genus, it is an integral over a curvature that is closely related to the Gaussian curvature [19].

A fundamental consequence of the topological classification of band structures, is the existence of gapless conducting states at the interface between two systems with a different value of the topological invariant. We can understand this feature by imagining an interface, where a system slowly interpolates as a function of the distance y between two states with a different Chern number. Since the topological invariant is changing, the energy gap has to vanish for some value of y. Therefore there will be gapless edge

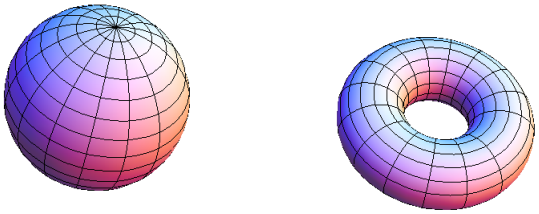

(A) Sphere (B) Torus

FIGURE 2.3: A sphere and a torus have a different genus; a torus has one hole and a sphere has none. They are therefore topologically different.

states bound to the region where the energy gap closes [19]. Unfortunately, most edge states are highly sensitive to disorder and therefore rarely survive on a macroscopic scale. However, topologically protected surface states are much more robust to perturbations of the Hamiltonian, and can be experimentally observed [25].

We have already discussed an example of topologically protected surface states, namely the Majorana edge modes in the Kitaev chain, which were protected by the particle-hole symmetry. How can surface states get topological protection in the Chern topological insulator? An important difference between the Chern topological insulator and the Kitaev chain that we presented before, is that the edge states are no longer zero-energy states localized at the zero-dimensional boundaries. Rather, they live on the one-dimensional edge of the system, and the corresponding state crosses the energy gap. Because of this crossing, the edge-states are conducting and called metallic. In the case of the two-dimensional Chern topological insulators, it turns out that the difference between the clockwise and counterclockwise propagating edge modes is in fact a topological invariant, equal to the Chern number. Thus, it cannot change under continuous deformations of the Hamiltonian, including changes that introduce disorder at the edges of the system, making the edge states topologically protected [26].

2.2.3 Time-Reversal Invariant Topological Insulators

In the case of topological Kondo insulators, the edge states are protected by time-reversal symmetry. This time-reversal symmetry also imposes that for every edge state, there is a backwards propagating partner. Thus, the Chern number is zero for Topological Kondo insulators, and we need a different topological invariant to define the underlying order: the spin Chern number which is a $\mathbb{Z}_2$ invariant. The identification and calculation of the bulk $\mathbb{Z}_2$ invariant is much more cumbersome than it is for Chern insulators. Luckily,

topological Kondo insulators exhibit inversion symmetry, which makes it relatively easy to calculate it's $\mathbb{Z}_2$ invariant [27]. In order to understand this calculation properly, we first need to understand what exactly is time-reversal symmetry, and how it leads to Kramers degeneracy. We will discuss this topic in the next subsection.

2.2.3.1 Time-Reversal Symmetry

Time reversal means that we apply the transformation $t \to -t$. In the classical case, this means that $x \to x$ and $p \to -p$. Since the spin is an angular momentum, spins flip under time reversal. Quantum mechanically, we say that a Hamiltonian has time-reversal symmetry if $THT^{-1} = H$. Here, $T = e^{i\pi S_y}K$, with S_y the total spin and K the complex-conjugation operator, generates the time-reversal operation. In the case of electron systems, it holds that $T^2 = e^{i2\pi S_y} = \pm 1$, depending on whether the total number of electrons in the system is even or odd. For electron systems, this leads to a constraint known as Kramers' theorem, which plays a vital role in the protection of edge states.

Since H and T commute, we have that for every eigenstate $|\Psi\rangle$ of the Hamiltonian, $T|\Psi\rangle$ is also an eigenstate with the same energy. This does not necessarily mean that all energy states are doubly degenerate. It could of course be that $|\Psi\rangle = T|\Psi\rangle$. However, in case $T^2|\Psi\rangle = -1|\Psi\rangle$, we can use

$$\langle T\Psi|T\Phi\rangle = (e^{i\pi S_y}|\Psi^*\rangle)^\dagger e^{i\pi S_y}|\Phi^*\rangle = \langle\Psi^*|e^{-i\pi S_y}e^{i\pi S_y}|\Phi^*\rangle = \langle\Psi|\Phi\rangle^*, \tag{2.8}$$

to find:

$$\langle T\Psi|\Psi\rangle^* = \langle T^2\Psi|T\Psi\rangle = -\langle\Psi|T\Psi\rangle = -\langle T\Psi|\Psi\rangle^*, \tag{2.9}$$

from which we can conclude that $\langle T\Psi|\Psi\rangle = 0$. Thus, $|\Psi\rangle \neq T|\Psi\rangle$ and we have doubly degenerate states [26]. This is known as Kramers theorem.

We can understand this behavior in terms of spin flip. Since eigenstates of the Bloch Hamiltonian are effective single-electron states, we see that the time-reversal operation flips the spin of this electron, thus $T|\Psi\rangle \neq |\Psi\rangle$, as they have opposite spin. It is important to notice that in the absence of spin-orbit interaction, Kramers' degeneracy is simply the degeneracy between up and down spins. However, in the presence of spin-orbit interaction, its consequences are non-trivial. Interestingly, a minimal model for a time-reversal invariant electronic insulator needs to have at least four energy bands. For a two band model, the energy bands would have to touch at the high-symmetry Γ_i points of the Brillouin zone in order to satisfy Kramers theorem, thus closing the energy gap [28].

Finally, we will discuss the consequences of time-reversal symmetry and Kramers theorem for the band structure of the Hamiltonian, since they play an important role in the protection of the edge states. A T-invariant Bloch Hamiltonian has to satisfy [19]

$$TH(k)T^{-1} = H(-k). \tag{2.10}$$

This means that if $|u(k)\rangle$ is an eigenvector of $H(k)$, with energy $E(k)$, then the other half of a so called Kramers pair $T|u(k)\rangle$ is also an eigenstate with the same eigenvalue $E(k) = E(-k)$ [28],

$$H(-k)T|u(k)\rangle = TH(k)T^{-1}T|u(k)\rangle = TH(k)|u(k)\rangle = TE(k)|u(k)\rangle = E(k)T|u(k)\rangle\,. \tag{2.11}$$

From this we find that the energy bands have to be symmetric with respect to inversion in the Brillouin zone, $k \to -k$. In d dimensions there are 2^d points Γ_i in the Brillouin zone that map to themselves under inversion. These points are located on the edges and in the middle of the Brillouin zone [26]. At these points, $TH(\Gamma_i)T^{-1} = H(\Gamma_i)$. Thus, using Kramers theorem, we find that these states exhibit a double degeneracy for the same k.

2.2.3.2 $\mathbb{Z}_2$ Invariant in Two Dimensions

The Kramers degeneracy does not only hold for the bulk states, but it is also true on the edges. This leads to a conservation of the parity of the number of edge-state Kramers pairs. In order to see this, we will now look at a two-dimensional time-reversal symmetric $T^2 = -1$ topological insulator. For a given dispersion relation, the number of edge-state Kramers pairs is well defined for any energy in the bulk gap. For example, we see that in figure 2.4 (A) there are three Krames pairs for every energy in the band gap. As disscused before, due to time-reversal symmetry, the band structure is symmetric under $k \to -k$, and thus there is an equal number of right- and left-moving states. If we now continuously deform the band structure to get rid of a Kramers pair, we see that we either have to remove two pairs at the same time, as depicted in figure 2.4 (B), or try to get rid of the pair that crosses $k_x = 0$. However, we cannot get rid of this Kramers pair in the same way, since this would make the states non degenerate on $k_x = 0$, which is a violation of Kramers theorem. Thus, we see that (without closing the bulk gap) we can only change the number of Kramers pairs in pairs, making the parity a topological invariant. This topological invariant is called the $\mathbb{Z}_2$ invariant and takes the value 1 (0) if the parity of Kramers pairs is odd (even) [26].

We have now defined the $\mathbb{Z}_2$ invariant by only looking at the edges of the system. However, its value does not depend on the type of edge, it is a topological invariant that

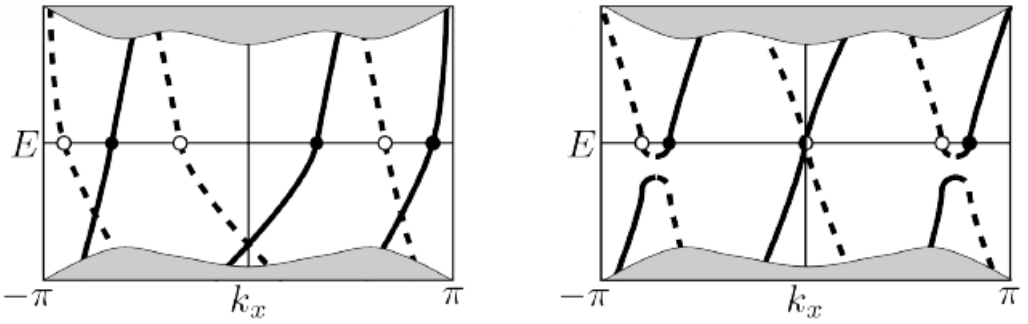

FIGURE 2.4: Schematic representation of the edge states in a two-dimensional time-reversal symmetric topological insulator with $T^2 = -1$. The bulk continuum states are depicted by the shaded regions. From (A) to (B), the system undergoes a continuous deformation, respecting the time-reversal symmetry. Right- (left-) propagating states are denoted by continuous (dashed) lines. Notice that crossings at $k = 0$ and $k = \pm\pi$ cannot become avoided crossings, as this would violate the Kramers theorem. Image source: [26].

is set by the bulk Hamiltonian. There should therefore be a topological invariant of the bulk Hamiltonian that corresponds to it. In the presence of inversion symmetry, we can calculate this relatively easily.

Similar to time reversal, inversion means that we apply the transformation $x \to -x$. Although this transformation does not flip the spin like time reversal, it does flip the momentum. We say that a Bloch system is symmetric under inversion if there exists a unitary operator P independent of k, such that:

$$P^\dagger P = 1; \tag{2.12}$$

$$P^2 = 1; \tag{2.13}$$

$$PH(k)P^{-1} = H(-k); \tag{2.14}$$

$$PT = TP. \tag{2.15}$$

Consider the time-reversal invariant momenta Γ_i. As discussed before, each eigenstate $|\Psi\rangle_i$ at these momenta has an orthogonal Kramers pair $T|\Psi\rangle_i$ with the same energy. Now, if H is inversion symmetric, we can choose $|\Psi\rangle_i$ to be an eigenstate for P as well, since $H(\Gamma_i)$ and P commute,

$$PH(\Gamma_i)P^{-1} = H(-\Gamma_i) = H(\Gamma_i). \tag{2.16}$$

Since $P^2 = 1$, we thus find that $P|\Psi\rangle_i = \pm|\Psi\rangle_i$. Because P and T commute, we have that the Kramers pair of $|\Psi\rangle$, $T|\Psi\rangle$ has the same parity eigenvalue [26]. In reference [27], it has been shown that these eigenvalues can be related to the $\mathbb{Z}_2$ invariant ν as

follows:

$$(-1)^{\nu} = \prod_{m=1}^{N} \prod_{i} \xi_{2m}(\Gamma_i). \tag{2.17}$$

Here, $\xi_{2m}(\Gamma_i) = \pm 1$ is the parity eigenvalue of the $2m$'th occupied band at Γ_i. Notice that the values $\xi_{2m-1}(\Gamma_i)$ are left out. Since they have the the same value as their Kramers pair $\xi_{2m}(\Gamma_i)$, including them would make the outcome trivial.

2.2.3.3 $\mathbb{Z}_2$ Invariant in Three Dimensions

We have now discussed the bulk-edge correspondence for two-dimensional time-reversal -and inversion- symmetric systems. However, the topological Kondo insulator is a three-dimensional material. In three dimensions a band structure with time-reversal symmetry is characterized by four $\mathbb{Z}_2$ invariants. The surface states of three of those are not robust in the presence of disorder, and for this reason they are referred to as weak-topological insulators. These weak-topological insulators can be seen as a stacking in one of the three spatial directions of the two-dimensional topological insulators that we discussed in the previous section. If two of these layers are coupled together, the total number of Kramer pairs becomes even, making them a simple insulator. Thus, it turns out that a stack of even layers is equivalent to an insulator, while an odd number of layers yields a (thicker) two-dimensional topological insulator. From this sensitivity to the parity of the number of layers, we can conclude that the weak-topological invariants do not characterize a robust topological phase [27].

The fourth $\mathbb{Z}_2$ invariant ν can be calculated using the formula (2.17) in the presence of inversion symmetry. $\nu = 1$ corresponds to a topological state with robust surface states, which is called a strong-topological insulator (STI). Unlike weak-topological insulators, a STI cannot be interpreted as a stacking of two-dimensional topological insulators. The robust surface states of a STI form a two-dimensional topological metal. A topological metal is not spin degenerate, like a normal metal, which has up and down spins at each point of the Fermi surface. Rather, since time-reversal symmetry requires that states at momenta k and $-k$ have opposite spin, the spin has to rotate around the Fermi surface during this operation [19].

2.2.4 The 10-Fold Way

As discussed before, we can use topological invariants to classify materials. We have now presented several topological models that were classified by different topological invariants. In general, we can say that topological materials are either classified by a $\mathbb{Z}_2$ invariant that can only assume two values, or a $\mathbb{Z}$ invariant that can have any integer

symmetry				dimension							
class	T	Ξ	Π	1	2	3	4	5	6	7	8
A	0	0	0	0	$\mathbb{Z}$	0	$\mathbb{Z}$	0	$\mathbb{Z}$	0	$\mathbb{Z}$
AIII	0	0	1	$\mathbb{Z}$	0	$\mathbb{Z}$	0	$\mathbb{Z}$	0	$\mathbb{Z}$	0
AI	1	0	0	0	0	0	$\mathbb{Z}$	0	$\mathbb{Z}_2$	$\mathbb{Z}_2$	$\mathbb{Z}$
BDI	1	1	1	$\mathbb{Z}$	0	0	0	$\mathbb{Z}$	0	$\mathbb{Z}_2$	$\mathbb{Z}_2$
D	0	1	0	$\mathbb{Z}_2$	$\mathbb{Z}$	0	0	0	$\mathbb{Z}$	0	$\mathbb{Z}_2$
DIII	-1	1	1	$\mathbb{Z}_2$	$\mathbb{Z}_2$	$\mathbb{Z}$	0	0	0	$\mathbb{Z}$	0
AII	-1	0	0	0	$\mathbb{Z}_2$	$\mathbb{Z}_2$	$\mathbb{Z}$	0	0	0	$\mathbb{Z}$
CII	-1	-1	1	$\mathbb{Z}$	0	$\mathbb{Z}_2$	$\mathbb{Z}_2$	$\mathbb{Z}$	0	0	0
C	0	-1	0	0	$\mathbb{Z}$	0	$\mathbb{Z}_2$	$\mathbb{Z}_2$	$\mathbb{Z}$	0	0
CI	1	-1	1	0	0	$\mathbb{Z}$	0	$\mathbb{Z}_2$	$\mathbb{Z}_2$	$\mathbb{Z}$	0

TABLE 2.1: The ten-fold way. The symmetries are specified by the absence or presence of time-reversal symmetry T, particle hole symmetry Ξ and chiral symmetry $\Pi = \Xi T$. ± 1 (0) denote the presence (absence) of symmetry, with ± 1 specifying the value of Ξ^2 and T^2. The symmetry classes are labeled using the notation of Altland and Zirnbauer (1997). Data source: [19].

value. The time-reversal invariant topological insulators that we just discussed, are an example of materials that are characterized by a non-trivial value of the $\mathbb{Z}_2$ invariant. We recall that the invariant could only have two different values, the parity of Kramers pairs was either odd or even. The Kitaev chain describes a topological superconductor that also has a $\mathbb{Z}_2$ invariant; it either has edge sates or not, there are no other topological phases. The Chern invariant, on the other hand, is an example of a $\mathbb{Z}$ invariant. The difference between left- and right-propagating particles is not restricted to zero and one, but it can have any integer value. Thus, the Chern insulator has infinitely many different topological phases. A topological invariant is meaningful only if it is possible to connect it to the surface states through a bulk-boundary correspondence, so that the edge states are topologically protected. As we just discussed for both the time-reversal invariant topological insulators and the Kitaev chain, symmetries play an important role in this process.

The ideas described above can be used to create an elegant mathematical structure, which generalizes the ideas of topological band theory. In this structure, classes of equivalent Hamiltonians are determined by specifying the symmetries and the dimensionality. Using the bulk-boundary correspondence, each of these classes can then be topologically classified by either $\mathbb{Z}_2$, $\mathbb{Z}$ or 0, where 0 signifies that the class has no topological behavior. This procedure leads to the periodic table of topological materials shown in table (2.1) [29–33]. Here, we indeed recognize the entry of a time-reversal invariant $T^2 = -1$, $\mathbb{Z}_2$ topological insulator in two and three dimensions (class AII), the Chern insulator without symmetries in two dimensions (class A), and the one-dimensional Kitaev chain with particle-hole symmetry (class D). This classification system is referred to as the ten-fold way, because we distinguish ten different symmetry classes. These classes arise

due to the three possibilities $(0, +1, -1)$ for both time-reversal and particle-hole symmetry, which together give $3 \times 3 = 9$ classes, in addition to the class of materials that are not symmetric under either a particle-hole switch or time-reversal, but are symmetric under a combination of them.

2.3 Topological Kondo Insulators

Now that we have acquired a better idea of what topological materials are, and how we can classify them, it is time to turn our attention to Kondo insulators. We will first introduce the concept of Kondo insulators, then we will consider topological Kondo insulators, and finally we will present a specific example of a possible candidate to be a topological Kondo insulator, namely samarium hexaboride (SmB_6).

2.3.1 Kondo Insulators

The interaction between conduction electrons and local moments is called the Kondo effect. In the Kondo effect, the low temperature behavior of a single local moment can be understood as the formation of a singlet bound state between the local moment and a conduction electron. As described in section 2.1, a Kondo insulator is then a state in which all the conduction electrons form a spin singlet bound state with the local moment of an impurity. The binding energy of the Kondo singlets is responsible for the band gap separating the conduction electrons from the conduction band and is related to the Kondo temperature T_k. Unfortunately, this picture is not quite complete, since in the limit where there are as much impurities as there are conduction electrons, the interaction between the local moments cannot be ignored [34].

2.3.1.1 Anderson Lattice Model

In order to incorporate these interactions, we will use the Anderson lattice model (ALM) [15]. This model, as well as the phenomenon of Anderson Localization, are both named after the physicist and Nobel Prize winner Philip Anderson. Although both of them can lead to a localization of conduction electrons, they are in fact quite different phenomena. Anderson localization occurs due to disordered impurities, but they do not need to be magnetic. In the ALM there is no disorder, since the impurities are placed on a lattice, but the magnetic moment of the impurities plays an important role. In the following, we will assume that the role of magnetic impurities is played by f-electrons (electrons in the f shell of an atom).

The ALM is described by a Hamiltonian that consists of three parts,

$$H_{ALM} = H_c + H_f + H_h. \tag{2.18}$$

The first part, H_c, describes the conduction electrons. In the most general case, there can be more than one conduction band, such that the Hamiltonian describing the conduction electrons becomes

$$H_c = \sum_{l,l'} \sum_{k,\sigma} \xi_{l,l'}(k) c^{(l)\dagger}_{k\sigma} c^{(l')}_{k\sigma}. \tag{2.19}$$

Here, $\xi_{l,l'}(k)$ is the dispersion between electrons of bands l and l', σ is the spin index, and $c^{(l)\dagger}_{k\sigma}$ is the creation operator of a conduction electron. The second part, H_f, describes the f-electrons, and is given by,

$$H_f = \sum_{i,j} \sum_{\alpha,\alpha'} \epsilon_{\alpha\alpha' ij} f^\dagger_{j\alpha} f_{i\alpha'} + U \sum_{i\alpha\alpha'} f^\dagger_{i\alpha} f_{i\alpha} f^\dagger_{i\alpha'} f_{i\alpha'}. \tag{2.20}$$

Here, $f^\dagger_{j\alpha}$ creates an f-electron on site j with pseudo spin α, $\epsilon_{\alpha\alpha' ij}$ is the hopping amplitude, and $U > 0$ is the strength of the interaction between the f-electrons. Due to the presence of strong spin-orbit coupling, α is not a spin index. Instead, it can be generally characterized by the total angular momentum J, and its z component M. The last part of the Hamiltonian H_h describes the hybridization between the conduction electrons and the f-electrons,

$$H_h = \sum_{l,i,\sigma} \sum_{j,\alpha} (V^{(l)}_{i\sigma,j\alpha} c^{(l)\dagger}_{i\sigma} f_{j\alpha} + H.c.), \tag{2.21}$$

where $V^{(l)}_{i\sigma,j\alpha}$ is the hybridization matrix element. It is important to note here that the hybridization is responsible for the opening of the band gap. Without the hybridization, the d- and f-bands would overlap, and the material would be metallic, as shown schematically in figure 2.5.

2.3.1.2 Slave-Boson Approximation

We will start from the ALM model to derive an effective model that is quadratic in the creation and annihilation operators. For this, we use the slave-boson approximation. In this approximation, we take the limit $U \to \infty$. Since the f bands in Kondo insulators are close to being completely filled, this corresponds to projecting out the states with two or more f holes per site. We impose this constraint by using slave bosons, and finally calculate the effective model by applying a mean-field approximation on the bosonic fields.

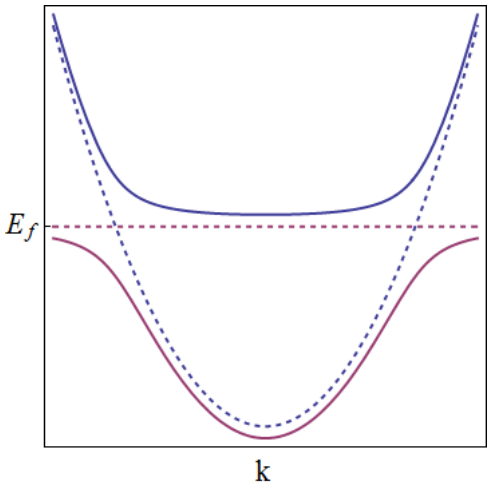

FIGURE 2.5: Schematic depiction of the band structure of a Kondo insulator. Without hybridization the bands overlap (dashed lines), when the hybridization is included (non dashed lines) a gap opens up at the Fermi energy, and the material becomes insulating.

First of all, we need to impose the constraint on the system. It turns out that in the case of almost filled f-bands (which is the case we consider later for SmB_6), this is most easily done by going to the hole representation. In this representation, $f^\dagger_{i\alpha}$ and $c^{(l)\dagger}_{i\sigma}$ create a hole at site i with (pseudo) spin (α) σ. Practically, going to the hole representation means that we transform creation operators into annihilation operators, and vice versa. Then, we reorder the Hamiltonian in the same form as before, and, by doing so, we observe that we have effectively only gained a minus sign. Thus, by going to the hole representation, we find that $H \to -H$.

We are now ready to introduce the slave bosons and impose the constraint of no more than one f hole per site. We assume that the slave boson is filling up the place of the f hole if it is not there, allowing us to impose the constraint by keeping the sum of the f holes and bosons equal to one. This means that if an f hole is created, a slave boson has to be annihilated and vice versa. Thus, we get the transformation,

$$f^\dagger_{\alpha i} \to f^\dagger_{\alpha i} b_i, \tag{2.22}$$

where b_i is the slave boson annihilation operator. This then enables us to formulate the constraint that projects out the doubly occupied states,

$$b^\dagger_i b_i + \sum_\alpha f^\dagger_{i\alpha} f_{i\alpha} = 1. \tag{2.23}$$

Due to the constraint in equation (2.23), $b_i^\dagger b_i$ and $f_{i\alpha}^\dagger f_{i\alpha}$ cannot be simultaneously nonzero, and consequently the slave bosons drop out for the on site energy,

$$f_{i\alpha}^\dagger b_i b_i^\dagger f_{i\alpha} = (1 + b_i^\dagger b_i) f_{i\alpha}^\dagger f_{i\alpha} = f_{i\alpha}^\dagger f_{i\alpha}. \tag{2.24}$$

Applying his transformation to the Hamiltonian in the hole representation and imposing the constraint using the Lagrange multipliers λ_i, we find,

$$H = -\sum_{l,l',k,\sigma} \xi_k^{l,l'} c_{k\sigma}^{(l)\dagger} c_{k\sigma}^{(l')} - \sum_{i,j} \sum_{\alpha,\alpha'} \epsilon_{\alpha\alpha' ij} f_{j\alpha}^\dagger b_j b_i^\dagger f_{i\alpha'} - \sum_{i,j,\alpha,\sigma,l} (V_{i\sigma,j\alpha}^{(l)} f_{j\alpha}^\dagger b_j c_{i\sigma}^{(l)} + H.c.) + \sum_j i\lambda_j \left(b_j^\dagger b_j + \sum_\alpha f_{j\alpha}^\dagger f_{j\alpha} - 1 \right). \tag{2.25}$$

Now, we can apply a mean-field approximation, in which we replace the b_i, $b_i^\dagger$ operators by their expectation values, $\langle b_i \rangle = \langle b_i^\dagger \rangle = b$, and $i\lambda_j$ by $\bar{\lambda}$, which gives us the effective Hamiltonian,

$$H = -\sum_{l,l',k,\sigma} \xi_k^{l,l'} c_{k\sigma}^{(l)\dagger} c_{k\sigma}^{(l')} - b^2 \sum_{i \neq j} \sum_{\alpha,\alpha'} \epsilon_{\alpha\alpha' ij} f_{j\alpha}^\dagger f_{i\alpha'} - \sum_i \sum_{\alpha,\alpha'} \epsilon_{\alpha\alpha ii} f_{i\alpha}^\dagger f_{i\alpha} - b \sum_{i,j,\alpha,\sigma,l} (V_{i\sigma,j\alpha}^{(l)} f_{j\alpha}^\dagger c_{i\sigma}^{(l)} + H.c.) + \sum_j \bar{\lambda} \left(b^2 + \sum_\alpha f_{j\alpha}^\dagger f_{j\alpha} - 1 \right). \tag{2.26}$$

After grouping together the $f_{i\alpha}^\dagger f_{i\alpha}$ terms, and performing the index independent summations, we find,

$$H_{eff} = -\sum_{k,\sigma} \xi_k^{l,l'} c_{k\sigma}^{(l)\dagger} c_{k\sigma}^{(l)} - \sum_{i,\alpha} (\epsilon_{i\alpha} - \bar{\lambda}) f_{i\alpha}^\dagger f_{i\alpha} - b^2 \sum_{i \neq j,\alpha,\alpha'} t_{ij\alpha\alpha'} f_{i\alpha}^\dagger f_{j\alpha'} - b \sum_{i,j,\alpha,\sigma} (V_{i\sigma,j\alpha}^{(l)} f_{i\alpha}^\dagger c_{i\sigma}^{(l)} + H.c.) + N_s (b^2 - 1)\bar{\lambda}, \tag{2.27}$$

where we have renamed the f-electron hopping to $t_{ij\alpha\alpha'}$ and N_s is the number of sites. In order to proceed, we have to calculate the values of b and $\bar{\lambda}$. This can be done by minimizing the free energy associated with the effective Hamiltonian [35]. We start by calculating the partition function Z, since the free energy F is given by $F = -k_B T \log Z$. Following the procedure given in reference [36], we have that

$$Z = \mathrm{Tr}\left(e^{-\beta H_{eff}} \right) = \int_{\Psi(0) = -\Psi(\hbar\beta)} \mathcal{D}(\bar{\Psi}, \Psi) e^{-S_{eff}/\hbar}, \tag{2.28}$$

where S_{eff} is the Euclidean action corresponding to H_{eff}, and is given by

$$S_{eff} = \int_0^{\hbar\beta} d\tau \left(\bar{\Psi} \partial_\tau \Psi + H_{eff} \left[\bar{\Psi}, \Psi \right] \right), \tag{2.29}$$

and $\Psi(k, \tau)$ denotes the fermionic coherent state. In case of two conduction electrons and two f-electrons, $\Psi = (\phi_{c\uparrow}, \phi_{c\downarrow}, \phi_{f\uparrow}, \phi_{f\downarrow})$. Performing a Fourier transformation to the momentum representation, we find that S_{eff} is given by

$$S_{eff} = \hbar\beta N_s (b^2 - 1)\bar{\lambda} - \int_0^{\hbar\beta} d\tau \sum_k \int_0^{\hbar\beta} d\tau' \sum_{k'} \bar{\Psi}(\tau, k) G^{-1}(\tau, k, \tau', k') \Psi(\tau', k'), \tag{2.30}$$

where G^{-1} denotes,

$$G^{-1}(\tau, k, \tau', k') = \begin{pmatrix} -\partial_\tau \underline{1} + \xi_k & b V_k^\dagger \\ b V_k & -\partial_\tau \underline{1} + (\epsilon_k - \bar{\lambda}\underline{1}) + b^2 t_k \end{pmatrix} \delta(k - k') \delta(\tau - \tau'). \tag{2.31}$$

Here $\underline{1}$ denotes the unitary matrix. Since S_{eff} is at most quadratic in Ψ, we can now perform the path integral in equation (2.28) to find,

$$Z = \exp\left[-\beta N_s (b^2 - 1)\bar{\lambda} + \mathrm{Tr} \log(-G^{-1})/\hbar \right]. \tag{2.32}$$

Now that we have found the partition function, we can calculate the free energy,

$$F = -k_b T \left[-\beta N_s (b^2 - 1)\bar{\lambda} + \mathrm{Tr} \log(-G^{-1})/\hbar \right]. \tag{2.33}$$

Since,

$$\frac{\partial}{\partial b} \left[\mathrm{Tr} \log(-G^{-1}) \right] = \mathrm{Tr} \left[-G \frac{\partial(-G^{-1})}{\partial b} \right] \tag{2.34}$$

$$= \mathrm{Tr} \left[\int_0^{\hbar\beta} \int_0^{\hbar\beta} d\tau d\tau' \sum_{k,k'} G(\tau, k, \tau', k') \frac{\partial}{\partial b} G^{-1}(\tau', k', \tau, k) \right] \tag{2.35}$$

$$= \mathrm{Tr} \left[\int_0^{\hbar\beta} \int_0^{\hbar\beta} d\tau d\tau' \sum_{k,k'} G(\tau, k, \tau', k') \begin{pmatrix} 0 & V_k^\dagger \\ V_k & 2bt_k \end{pmatrix} \delta(k - k') \delta(\tau - \tau') \right] \tag{2.36}$$

$$= \mathrm{Tr} \left[\int_0^{\hbar\beta} d\tau \sum_k G(\tau, k, \tau, k) \begin{pmatrix} 0 & V_k^\dagger \\ V_k & 2bt_k \end{pmatrix} \right] \tag{2.37}$$

$$= \mathrm{Tr} \left[\hbar\beta \sum_k G(\tau, k, \tau, k) \begin{pmatrix} 0 & V_k^\dagger \\ V_k & 2bt_k \end{pmatrix} \right], \tag{2.38}$$

where in the last step we used that $G(\tau, k, \tau', k)$ only depends on k and $\tau - \tau'$, we can now minimize this free energy with respect to b to find,

$$0 = bN_s\bar{\lambda} - \sum_k \mathrm{Tr}\left[\left\langle f_k^\dagger c_k \right\rangle V_k\right] - b\sum_k \mathrm{Tr}\left[\left\langle f_k^\dagger f_k \right\rangle t_k\right]. \tag{2.39}$$

Here, we have used the notation,

$$G(\tau, \tau, k, k) = \begin{pmatrix} \left\langle c_k^\dagger c_k \right\rangle & \left\langle c_k^\dagger f_k \right\rangle \\ \left\langle f_k^\dagger c_k \right\rangle & \left\langle f_k^\dagger f_k \right\rangle \end{pmatrix}. \tag{2.40}$$

Similarly, minimizing with respect to λ, we find, as expected, the averaged constraint condition,

$$1 = b^2 + \frac{1}{N_s}\sum_{k,\alpha}\left\langle f_{k\alpha}^\dagger f_{k\alpha}\right\rangle. \tag{2.41}$$

As discussed before, for a Kondo insulator, we are looking specifically at the regime where the number of holes per site is equal to the number of conduction bands N_d. This gives the additional constraint [11],

$$N_d = \frac{1}{N_s}\sum_{k,\alpha}\left\langle f_{k\alpha}^\dagger f_{k\alpha}\right\rangle + \frac{1}{N_s}\sum_{k,l,\sigma}\left\langle c_{k\sigma}^{(l)\dagger} c_{k\sigma}^{(l)}\right\rangle. \tag{2.42}$$

Before we can use these equations to calculate the values of b, λ and μ, we first need to find an expression for the Green's functions (the two-point expectation values).

2.3.1.3 Calculation of the Green's Functions

In order to calculate the Green's functions, we first investigate what happens when the Hamiltonian is diagonal in the Ψ_k basis ($H = \sum_k \Psi_k^\dagger D \Psi_k$, with D a diagonal matrix). In that case, we have that

$$\mathrm{Tr}(e^{-\beta H}) = \sum_{n_{1k_1}=0}^{1}\sum_{n_{2k_1}=0}^{1}\cdots\sum_{n_{nk_n}=0}^{1}\langle 0|\prod_{j,k}(\Psi_{jk}^{n_{jk}})e^{-\beta H}\prod_{jk}(\Psi_{jk}^{\dagger n_{jk}})\,|0\rangle \tag{2.43}$$

$$= \sum_{n_{1k_1}=0}^{1}\sum_{n_{2k_1}=0}^{1}\cdots\sum_{n_{nk_n}=0}^{1} e^{-\beta\sum_{j,k} n_{jk}\epsilon_{jk}} \tag{2.44}$$

$$= \prod_{j,k}\left[\sum_{n_{jk}=0}^{1} e^{-\beta n_{jk}\epsilon_{jk}}\right], \tag{2.45}$$

$$\tag{2.46}$$

where ϵ_{jk} is the jth eigenvalue of the matrix H_k. In the same way, it holds that

$$\mathrm{Tr}(\Psi_{ik}^{\dagger}\Psi_{ik}e^{-\beta H}) = \prod_{j,k'\neq i,k}\left[\sum_{n_{jk'}=0}^{1} e^{-\beta n_{jk'}\epsilon_{jk'}}\right]\sum_{n_{ik}=0}^{1} n_{ik}e^{-\beta n_{ik}\epsilon_{ik}}. \tag{2.47}$$

Thus, we finally find the well known Dirac distribution,

$$\left\langle \Psi_{ik}^{\dagger}\Psi_{ik}\right\rangle = \frac{Tr(\Psi_{ik}^{\dagger}\Psi_{ik}e^{-\beta H})}{Tr(e^{-\beta H})} \tag{2.48}$$

$$= \frac{\sum_{n_{ik}=0}^{1} n_{ik}e^{-\beta n_{ik}\epsilon_{ik}}}{\sum_{n_{ik}=0}^{1} e^{-\beta n_{ik}\epsilon_{ik}}} \tag{2.49}$$

$$= \frac{1}{1+e^{\beta\epsilon_{ik}}}. \tag{2.50}$$

Unfortunately, the effective Hamiltonian we found in the previous sections is not diagonal in (pseudo)-spin space. We therefore have to apply a change of basis. If H_k is not diagonal for some basis C_k, we can relate this basis to another basis Ψ_k in which the Hamiltonian is diagonal, by the unitary matrix of eigenvectors S_k,

$$C_k = S_k\Psi_k. \tag{2.51}$$

For the elements of C_k this means,

$$C_{ki} = \sum_{\alpha} S_{i\alpha k}\Psi_{\alpha k}. \tag{2.52}$$

Thus, we find that for a non diagonal basis C_k,

$$\begin{aligned}\left\langle C_{jk}^{\dagger}C_{ik}\right\rangle &= \left\langle \sum_{\alpha\alpha'} S_{j\alpha k}^{*}\Psi_{\alpha_k}^{\dagger}S_{i\alpha' k}\Psi_{\alpha' k}\right\rangle \\ &= \sum_{\alpha\alpha'} S_{j\alpha k}^{*}S_{i\alpha' k}\left\langle \Psi_{\alpha k}^{\dagger}\Psi_{\alpha' k}\right\rangle \\ &= \sum_{\alpha} S_{j\alpha k}^{*}S_{i\alpha k}\left\langle \Psi_{\alpha k}^{\dagger}\Psi_{\alpha k}\right\rangle \\ &= \sum_{\alpha} S_{j\alpha k}^{*}S_{i\alpha k}\frac{1}{1+e^{\beta\epsilon_{\alpha k}}},\end{aligned} \tag{2.53}$$

where we used that $\left\langle \Psi_{\alpha k}^{\dagger}\Psi_{\alpha' k}\right\rangle = \left\langle \Psi_{\alpha k}^{\dagger}\Psi_{\alpha k}\right\rangle \delta_{\alpha,\alpha'}$. Thus, if we have a Bloch Hamiltonian H_k, we can now calculate the Green's function from the eigenvalues and eigenvectors of H_k [16]. These steps finally allow us to numerically evaluate all parts of the mean-field equations, reducing their solution to a purely numerical problem. We will discuss the

numerical procedure in the chapter 5.

2.3.2 Topological Kondo Insulators

The next question at this point is: when does the effective model derived above describe a topological Kondo insulator? In order to answer this question, we can use equation (2.17) to calculate the $\mathbb{Z}_2$ invariant. However, before we can apply this formula, we need to calculate the eigenvalues of the parity operator. Since the parity of the conduction (d) electrons is 1 and the parity of the f-electrons is -1, we have that the operator for parity P is,

$$P = \begin{pmatrix} \underline{1}_d & \\ & -\underline{1}_f \end{pmatrix}. \tag{2.54}$$

Here, $\underline{1}_{d(f)}$ is the unitary matrix with the dimensionality of the amount of $d(f)$ electron bands in the model. We see that $H_{eff}(k)$ only satisfies inversion symmetry ($H_{eff}(k) = PH_{eff}(-k)P^{-1}$) if V_k is antisymmetric under k reversal. When we assume inversion symmetry, this implies that V_k is zero at the high-symmetry points Γ_i, depicted in figure 2.6. At these points, the Hamiltonian therefore separates into two blocks,

$$H_{\Gamma_i} = \begin{pmatrix} H_{\Gamma_i d} & \\ & H_{\Gamma_i f} \end{pmatrix}. \tag{2.55}$$

Because of the shape of the parity operator P, this means that for an eigenstate corresponding to an eigenstate of $H_{\Gamma_i d(f)}$, the parity eigenvalue will pe positive (negative). Looking again at formula (2.17), we conclude that the $\mathbb{Z}_2$ invariant ν is only non-trivial if the sum of occupied f band Kramers pairs over all high-symmetry points is odd.

In case of two conduction electrons and two f-electrons, and a spin diagonal $H_{d(f)}$, this reduces to

$$(-1)^{\nu} = \prod_i sgn(\epsilon_{\Gamma_i d} - \epsilon_{\Gamma_i f}), \tag{2.56}$$

where $\epsilon_{\Gamma_i d(f)}$ is the eigenvalue with multiplicity two of $H_{d(f)}$. Thus, in this case, a Kondo insulator is a strong topological insulator if $sgn(\epsilon_{\Gamma_i d} - \epsilon_{\Gamma_i f})$ is negative for an odd number of high-symmetry points [15].

2.3.2.1 Surface-State Calculation

In order to check whether the calculations outlined above are correct, and edge states indeed appear in the topologically non-trivial regime, we will calculate the band structure of a system with boundaries. We can implement a boundary by Fourier transforming

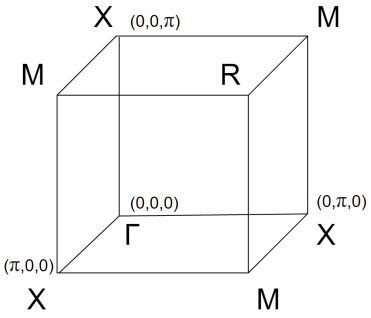

FIGURE 2.6: High-symmetry points in the Brillouin zone.

one of the components of the momentum vector to position space and making this space finite without periodic boundary conditions. In this way, we effectively get a stack of two-dimensional infinite planes.

In the case of two d-electron and two f-electron bands, this has been done in reference [15]. Here, the assumed dispersion relations are $\xi_k = -2t\sum_a \cos(k_a)$ and $\tilde{\epsilon}_f = -2t_f\sum_a \cos(k_a) + \mu_f$, where all energies have been taken relative to the chemical potential of the conduction electrons, which has been set to zero. We see that high-symmetry points labeled by the same letter in figure 2.6 yield an equal contribution to the topological invariant from equation (2.17). Assuming $t_f = 0.1t$, $\mu_f < 0$ (which has to be true for the model to be an insulator), and $t > 0$, we find that the R and X points always give a positive-signed contribution to the topological invariant. Thus, the topological invariant is completely determined by the contribution from the Γ and M points. We have that Γ gives a negative contribution if $-6(t - t_f) < \mu_f$, and M gives a negative contribution if $-2(t - t_f) < \mu_f$. Thus we find that the material is topological if

$$-6(t - t_f) < \mu_f < -2(t - t_f). \tag{2.57}$$

In order to see the edge states, we now consider a finite system, namely a stack of 32 two dimensional Kondo-insulator planes described by the Fourier transformation of the assumed dispersion relations and a hybridization of the form

$$V_k = \begin{cases} V(\sigma_x \sin k_x + \sigma_z \sin k_y), & \text{within the planes,} \\ iV_z\sigma_z, & \text{upwards between the planes,} \\ -iV_z\sigma_z, & \text{downwards between the planes,} \end{cases} \tag{2.58}$$

as in reference [15]. Calculating the eigenvalues of this Hamiltonian for different values of k_x, we indeed find gapless edge states as depicted in figure 2.7 for parameters in the topological regime. This band structure is similar to the one found in reference [15]; the

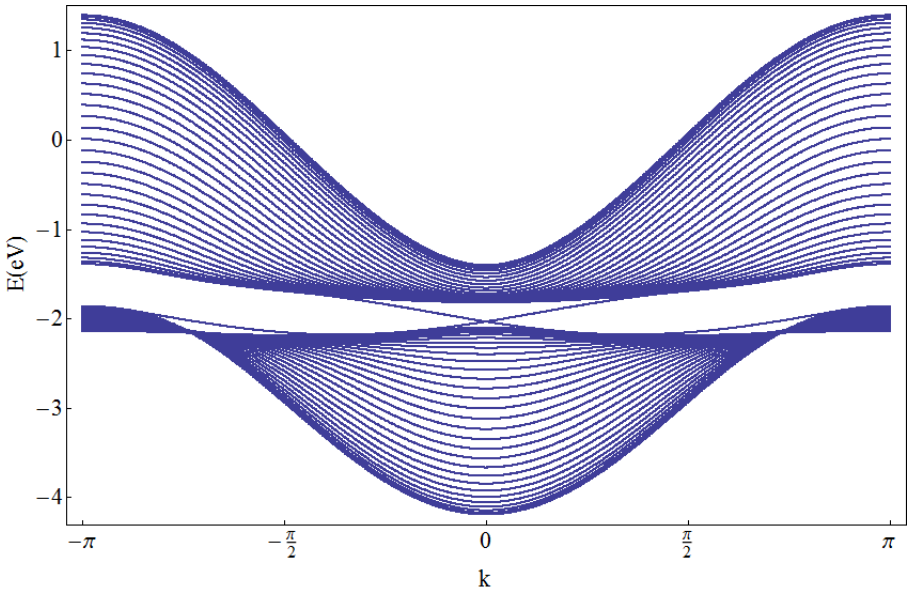

FIGURE 2.7: Band structure of a strong topological Kondo insulator with two fold degeneracy in the f levels, plotted along the x axis $k = k_x$, $k_y = 0$. We see a Dirac point inside the band gap as in reference [15]. The parameter values used are $t = 0.7$eV, $t_f = 0.1t$, $\mu_f = -2$eV, $V = 0.4$eV, and $V_z = 0.2$eV.

slight differences are probably due to the use of different parameter values (not specified in reference [15]).

2.3.3 Samarium Hexaboride

Samarium hexaboride SmB_6, is the first material proposed to be a Kondo insulator, and has been discovered almost fifty years ago [3]. The resistivity of SmB_6 as a function of temperature is shown in figure 2.8a. This closely resembles the resistivity one would expect from a Kondo insulator. At high temperatures it is a metal, and with decreasing temperature the material becomes insulating. Surprisingly, the resistivity does not diverge as the temperature goes to zero, there seems to be a residual conductivity as the temperature goes to zero. This effect is not understood in the Kondo insulator model and was originally explained by the presence of bulk impurities [3]. However, improvement of the sample quality did not seem to reduce this conductivity [3, 4]. In 2010 Dzero et al. [5] predicted that with the right configuration of parameters, topologically protected metallic surface states could form in the Kondo gap, producing a natural explanation for the saturated resistance [25]. Detailed band-structure calculations of SmB_6 followed, confirming that theoretically the material indeed had a non-trivial topological index [37, 38]. This resulted in a large amount of experimental research trying to confirm the existence of topological edge states in SmB_6. We will briefly discuss two types of these experiments (transport and ARPES) below.

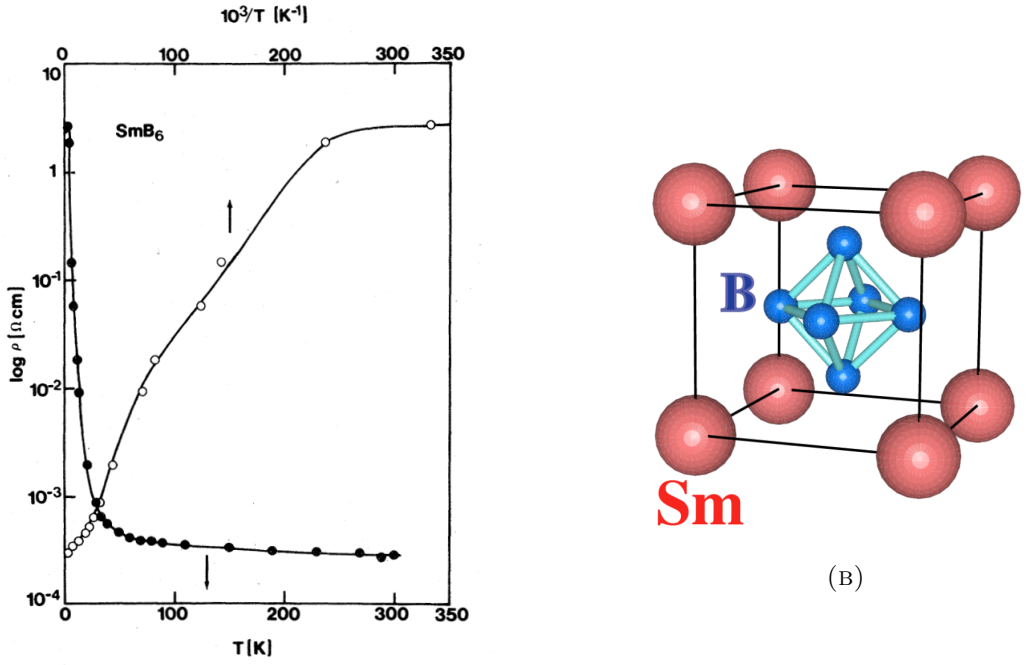

(A) (B)

FIGURE 2.8: (A) SmB_6 resistivity. As the temperature is lowered, SmB_6 turns into a Kondo insulator and the resistivity increases exponentially. However, at about 4 Kelvin the exponential growth of resistivity halts and we are left with a residual conductivity in the low-temperature regime. Image source: [4]. (B) Crystal structure of SmB_6. Image source: [37]

Transport studies constitute a very important tool in the search for an experimental proof of a topological phase in SmB_6. By using various sample sizes with different bulk surface ratios these type of experiments may reveal whether the residual conductivity is coming from the boundary or the bulk. As was reported in references [39], [40] and [41], there is virtually no residual bulk conductivity, strongly supporting the conclusion of topological edge states.

In addition, several angle resolved photo-emission (ARPES) studies have confirmed that there are in-gap metallic states [2, 42–46], as shown in figure 2.9. These ARPES results matched the theoretical prediction for the edge states from references [37, 38] remarkably well [42]. Combined with the transport studies, this seems consistent with the prediction of topological edge states. However, alternative explanations of the ARPES results have been proposed by Zhu et al. [47], casting doubts on whether the measured edge states were topological. Spin-resolved ARPES is seen as one of the most important methods to solve the controversy [25], since it would reveal whether the edge states are indeed spin momentum locked, as expected if the states are topological. In 2014, it was indeed shown by Xu et al. that the surface state around the X point in the surface Brillouin zone is spin-momentum locked [48], the results of this experiment are shown in figure 2.10. Here we see that along a cut through the Fermi surface at $k_x = 0$ the electrons are indeed

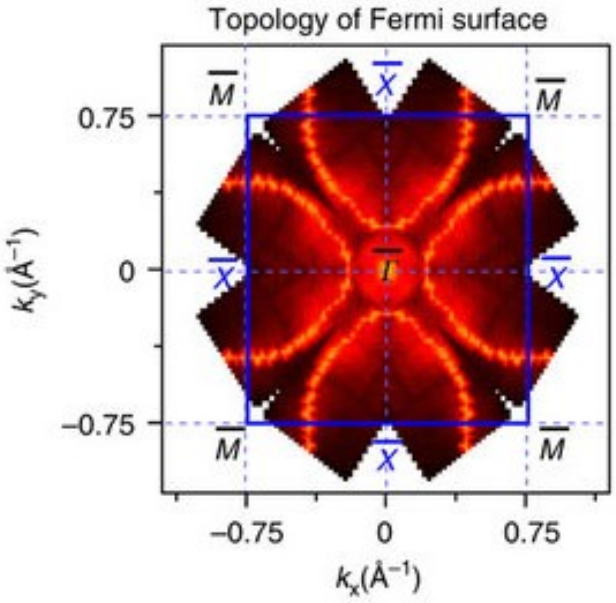

FIGURE 2.9: Fermi surface map of SmB_6 by Neupane et al. [42], using a laser based ARPES system. A more yellow color indicates a higher intensity. Intensity contours around the Γ and X points reflect in gap surface states that are consistent with the theoretical predictions.

spin momentum locked in the x direction (2.10 c,d) and not in the y and z direction (2.10 e-h), as expected from topological surface states. Although this finally seemed to be conclusive evidence for topological edge states, new research by Hlawenka et al. suggest that the edge states are not topological at all, but rather trivial surface states [49]. This interpretation however, is inconsistent with results from STM measurements of references [50], [51] and [52]. The solution of the controversy is believed to be in spin resolved ARPES measurements of the Dirac cone around the Γ point and an STM measurement of the quasi particle interference pattern. Unfortunately, these experiments have not yet been preformed successfully [6].

It is worth noticing that there have been several other important results that provide further evidence that the edge states are non-trivial. One of them is the ARPES experiment mentioned before by Neupane at al. [42], where it is shown that there are not only in-gap edge states, but that these states are also robust against thermo-cycling, as one would expect from a topological edge state. Another important result is that the edge states are robust against non-magnetic Y impurities, but destroyed by a similar amount of magnetic Gd impurities [39]. This difference in impurity endurance is naturally explained in the context of topological states, since magnetic impurities damage time-reversal symmetry.

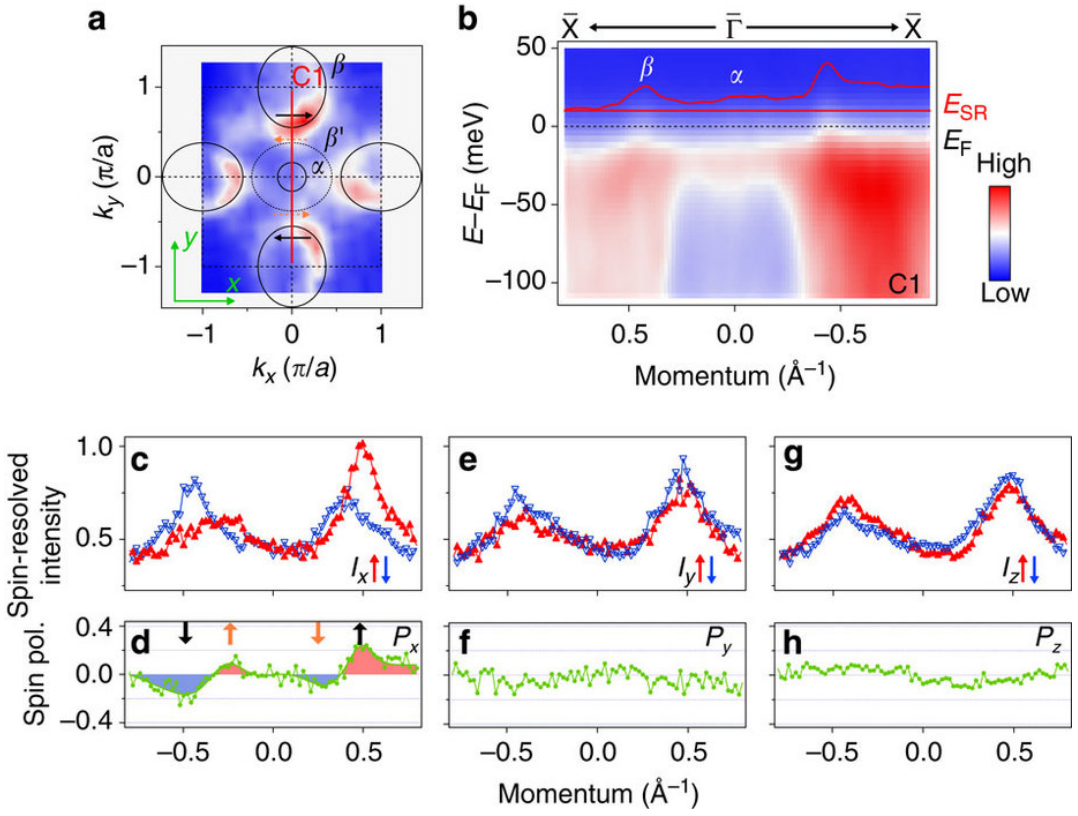

FIGURE 2.10: (a) Fermi surface map of SmB_6. (b) Intensity along the line C1 indicated in a, for different energies. The red curves indicate the position of the energy E_{SR} and the intensity at this energy level. (c) Spin resolved intensity projected on the x direction at E_{SR} along the line C1. The red and blue symbols indicate the spin up and spin down intensities respectively. (d) Spin polarization along the x direction for the momenta on C1 at energy E_{SR}. (e,f) Same as c, d but along the y direction instead. (g,h) same as c, d but along the z direction. Figure source: [48].

2.3.3.1 Band Structure

Although there is still no conclusive evidence for the topological nature of the edge states in SmB_6, this material is, to date, the most promising candidate for a topological Kondo insulator, which would be the first fully bulk-gapped, three-dimensional topological insulator [6]. Therefore, it is important to study the theoretical models proposed for the system, to explore further theoretical predictions that could potentially lead to meaningful experimental results, able to settle the dispute.

The first model proposed to describe a topological Kondo insulator was discussed in section 2.3.2.1. This model is the simplest model that we can imagine, that captures the essential features of a Kondo insulator. It has two d-electron bands (spin up and spin down), two f-electron bands (pseudo spin up and down), and (as we can see from the Hamiltonian transformed to position space), only nearest-neighbor hopping is taken

into account. Unfortunately, this does not completely capture the behavior of SmB_6, as the phase diagram is heavily dependent on the amount of f bands that are taken in to account, as shown in figure 2.11 [11]. In these phase diagrams we indeed see a topological phase transition from topological insulator to band insulator. In the next chapter we will discuss how this phase transition can be detected using a thermodynamic approach instead of calculating the changing topological invariant. In chapter 5 a similar phase diagram is calculated for a model with 6 f-bands. Although this phase diagram shows the same phases as the one in figure 2.11, it has a slightly different shape. The difference is probably caused by little differences in the model and a different method for solving the mean-field equations,as will be discussed in chapter 6.

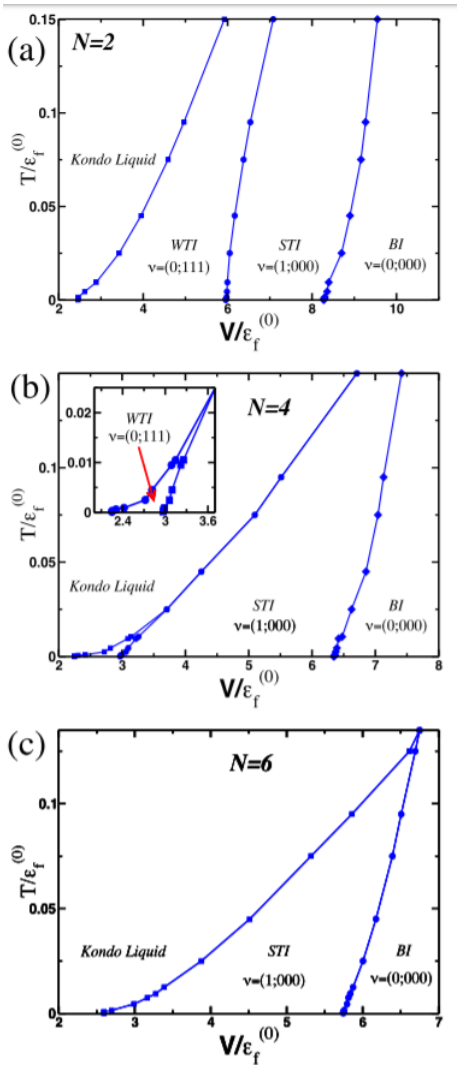

FIGURE 2.11: Phase diagrams of Kondo insulators for (a) two, (b) four and (c) six f bands. As the amount of f bands increases the weak topological insulator phase disappears. Figure source: [11].

As shown in references [11] and [53], the inclusion of the extra f bands also causes an increase of the parameter space in which the model predicted the existence of a

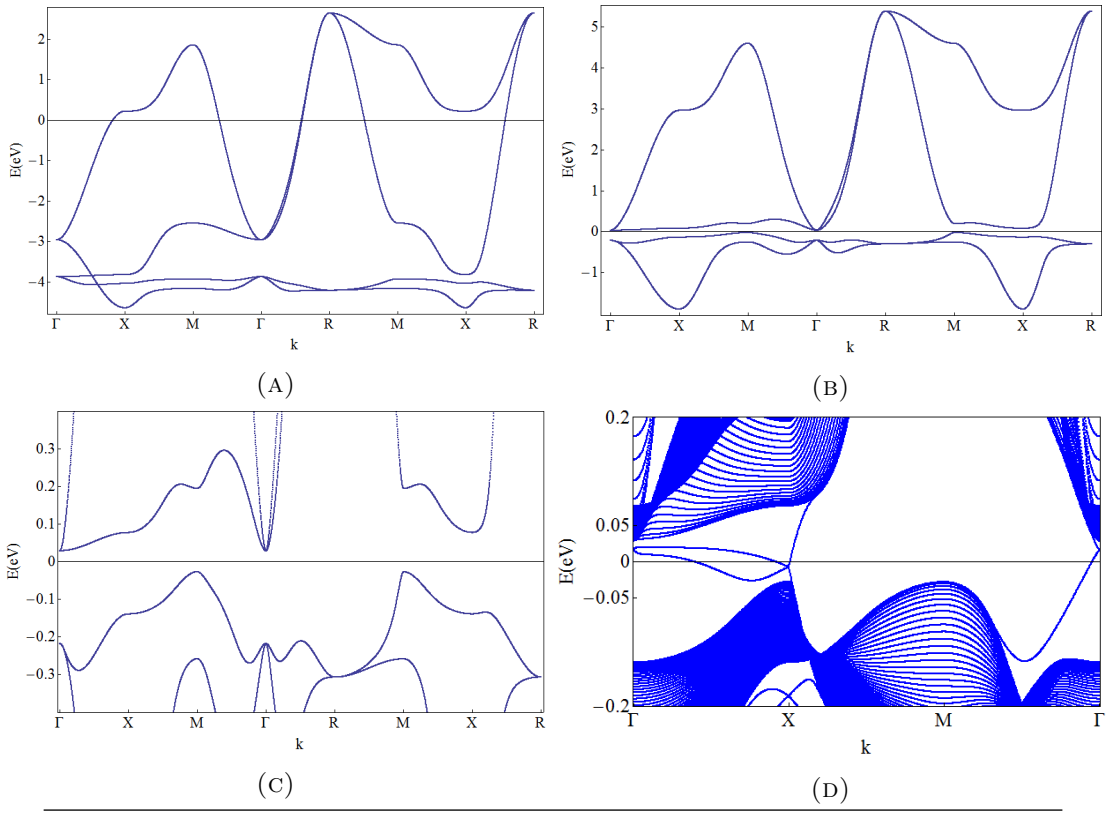

FIGURE 2.12: (A)Band structure of the model proposed in reference [37]. The structure does not have a gap. (B) Due to a shift in the on-site f-electron energy a gap arises, this can be seen more clearly in the zoomed-in image shown in (C). (D) Edge states appearing for the finite model of n=64 layers.

strong topological insulator. We have independently reproduced the band structure that corresponds to the model proposed by Tetsuya Takimoto in reference [37], which includes four d- and four f-bands, as shown in figure 2.12a. Unfortunately, the spectrum does not exhibit a gap. However, as proposed in the reference, we modified the on-site f-band energy levels such that $\epsilon_f/t_d = -4.06$ to open up an indirect gap. The resulting band structure is shown in figure 2.12b, where we also applied an overall energy shift to center the gap around zero energy. In figure 2.12d, we calculated the band structure for a finite-sized version of the model. As expected, we see the appearance of edge states.

The models in references [37] and [53] only take into account first nearest-neighbor hopping in the hybridization. However, in order to give a more quantitative comparison with experiments, a bit more effort is needed. In reference [16], six f bands an four d bands are included and the influence of terms up to seven nearest neighbor are investigated. The parameter values are chosen based on the results from ab-initio calculations [54]. The resulting band structure agrees semi-quantitatively with experimental results for SmB_6. A minimal model that captures the main features of the system is proposed. We have calculated the band structure for both the finite and infinite system described by this more elaborated model, and found the results shown in figures (2.13a), (2.13b),

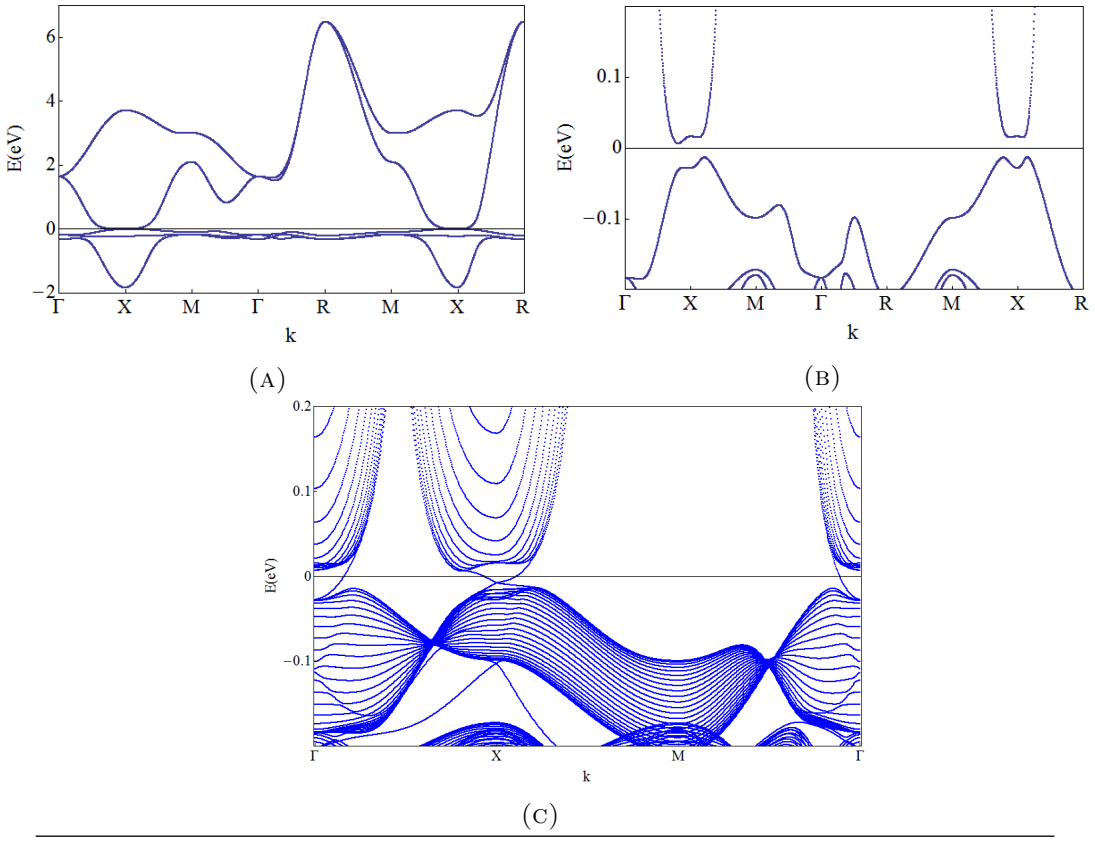

FIGURE 2.13: (A)Band structure of the minimal model proposed in reference [16] with inclusion of all hybridization terms up to second nearest neighbor, with mean field solutions $\lambda = 0.53$, $b = 0.76$ and $\mu = 0.15$ obtained using the method outlined in chapter (5). The structure has very small gap, as can be seen in the zoomed-in image shown in (B). (C) Edge states appear for the finite model of n=25 layers, at both the Γ and X points.

and (2.13c). Indeed, upon the inclusion of more bands, non-trivial edge states appear at both the Γ and the X points.

Now that we have a model of a topological Kondo insulator, and can calculate when this model is in a topological phase, we next need to calculate the thermodynamics of this model in order to calculate the heat capacity and phase transitions. We will discuss this in the next chapter.

Thermodynamics of Finite Systems

Generally, thermodynamics is used to describe a system in the thermodynamic many particle limit, such that the boundaries of the system are no longer relevant for the behavior of the system. In case of topological insulators however, we are interested in precisely these boundaries. In order to still use the principles of thermodynamics in systems where the boundaries are important, there are two different approaches available that eventually yield the same results in first order approximation; Hill thermodynamics and the traditional Gibbs method of effective boundary theories [55]. We will first review some basic thermodynamic concepts. In the following section we will consider the perhaps more intuitive Gibbs approach to include the boundaries of a system. After that, Hill thermodynamics will be investigated and we will discuss how Hill thermodynamics connects to the Gibbs approach as a more general form of the same physics. Finally, we will consider how the formalism can be applied to the SmB_6 model described in the previous chapter to calculate the heat capacity, detect phase transitions and determine their order.

3.1 Basic Thermodynamics

We will first consider the general thermodynamic formalism. The first law in thermodynamics is the thermodynamic identity

$$dE = TdS - pdV + \mu dN, \tag{3.1}$$

where E is the energy of the system, T the temperature, S the entropy, p the pressure, V the volume of the system, μ the chemical potential and N the particle number. Under the assumption that E is extensive in S, V and N this can easily be integrated to give

$$E = TS - pV + \mu N. \tag{3.2}$$

Unfortunately, in case of topological insulators, the boundary of the system should not be neglected, as this is exactly where the edge states are. This means that energy is no longer extensive in V, since if the volume doubles, the surface does not do the same. It is therefore no longer possible to straight forwardly perform the integration of equation (3.1), and a different approach becomes necessary, this problem is solved by Gibbs and Hill thermodynamics.

3.2 Gibbs Effective Boundary Theory

In Gibbs effective boundary theory, the boundary of the system is threated as an extensive thermodynamic variable in itself [55, 56]. The surface is threated as a separate thermodynamic system, with its own energy, entropy and particle number. Thus, for a system with bulk B and boundary b, we do not only have a bulk energy E_B,

$$E_B = S_B T_B - \nu V + N_B \mu_B, \tag{3.3}$$

there is also the boundary energy E_b,

$$E_b = S_b T_b - \gamma A + N_b \mu_b, \tag{3.4}$$

where A is the surface area. If the system is in thermodynamic equilibrium, we have that $T_B = T_b = T$ and $\mu_B = \mu_b = \mu$, and the total energy E becomes

$$E = T(S_B + S_b) - \nu V - \gamma A + \mu(N_B + N_b). \tag{3.5}$$

We can now determine the total grand potential Φ by summing the boundary and bulk grand potential ($\Phi_i = U_i - S_i T_i - \mu_i N_i$),

$$\Phi = -\nu V - \gamma A. \tag{3.6}$$

The corresponding thermodynamic identity reads,

$$d\Phi = -S dT - N d\mu - \nu dV - \gamma dA. \tag{3.7}$$

In case of constant temperature and chemical potential, the parameters γ and ν can be calculated by determining how the grand potential changes with different scalings. For example, in case of a three-dimensional system, that is periodic in two dimensions and non-periodic in the third, the grand potential can be calculated for different volumes, while keeping the surface constant by varying the length of the system in the non-periodic direction. Since the grand potential scales linearly with the volume, a linear fit through these points then gives both ν and γ. A problem with this formalism, is that it only works when the boundary and bulk are completely separated. In the case of a system with one finite dimension, this limit means that there can be no interaction between the top and bottom surface through the bulk, thus the separation between the two boundaries has to be long enough. Hill thermodynamics, on the other hand, does not impose this constraint at the start, and only yields the same results as Gibbs method for the grand potential if the constraint is imposed explicitly.

3.3 Hill Thermodynamics

Hill thermodynamics is based on the idea of introducing a new variable in the system, by allowing the number of systems to vary. We consider $\mathcal{N}$ identical copies of the system, each containing N particles. If we allow this number of identical copies to vary, the thermodynamic identity for the total system reads

$$dE_t = TdS_t - p\mathcal{N}dV + \mu dN_t - \hat{p}Vd\mathcal{N}, \tag{3.8}$$

here, the sub-script t stands for the total system, V is the volume of a single subsystem, and $-\hat{p}V$ is the thermodynamic response to a change in $\mathcal{N}$. It is important to notice here that $\hat{p}$ might in principle depend on V, however, the leading therm in $\hat{p}$ should always be linear in V. If we now consider a system with constant T, V, μ we can straightforwardly integrate equation (3.8), since it is extensive in $\mathcal{N}$, to find

$$E_t = TS_t - \hat{p}V\mathcal{N} + \mu N_t. \tag{3.9}$$

The energy of a single subsystem can now be recovered by dividing by the number of systems $\mathcal{N}$ to find

$$E = TS - \hat{p}V + \mu N, \tag{3.10}$$

here we used that $S = S_t/\mathcal{N}$ and $N = N_t/\mathcal{N}$. Since this result holds for any V, T, μ, we have effectively integrated equation (3.1) without assuming extensivity in V. This nonextensive behavior is expressed in the parameter $\hat{p}$ that can depend on V. Since $\hat{p}V$ has a leading term of order V we can rewrite the energy in the more recognizable form

$$E = TS - pV + \mu N + X, \tag{3.11}$$

where X is defined as $(p - \hat{p})V$ [14, 55].

In the case of the system with periodic boundary conditions in all but one direction that is large enough to separate bulk and boundary (as was discussed in the previous section), we see that $X = \gamma A$. However, Hill thermodynamics is also true if bulk and boundary are not separated, in which case X would include more sub-linear terms. Thus, we observe that although the Hill and Gibbs approach give the same results, Hill thermodynamics is applicable to a wider range of systems.

3.4 Application to SmB_6

We can now apply the formalism of finite-size systems to the finite form of the models described in section 2.3.3.1. In this case, we again have a model with periodic boundary conditions in all but one direction (the z direction). In the non-periodic direction the system consists of n layers. If n is large enough, there is no bulk-mediated interaction between the upper an lower layer, and equation (3.6) can be applied. Thus the grand potential can be separated in a boundary and a bulk contribution

$$\Phi(T, n, l) = \phi_0(T)l^2 + \phi(T)nl^2, \tag{3.12}$$

where l is the number of sites in the periodic directions, $\phi_0(T)$ is the contribution of the surface to the grand potential and $\phi(T)$ is the volume contribution. If l is kept constant for a calculation of the grand potential, then so is the surface. Using,

$$\Phi(T, n, l) = \frac{1}{\beta} \log\left(\mathrm{Tr}\left[e^{-\beta H}\right]\right) \tag{3.13}$$

$$= \frac{1}{\beta} \log\left(\prod_{j,k}\left[\sum_{n_{jk}=0}^{1} e^{-\beta n_{jk}\epsilon_{jk}}\right]\right) \tag{3.14}$$

$$= \frac{1}{\beta} \sum_{j,k} \log\left(1 + e^{-\beta\epsilon_{jk}}\right) \tag{3.15}$$

to calculate the grand potential for several values of n, $\phi_0(T)$ and $\phi(T)$ can be determined by making a linear fit to the function [55],

$$\frac{\Phi(T, n, l)}{l^2} = \phi_0(T) + \phi(T)n. \tag{3.16}$$

Using this grand potential, the order and location of the topological phase transition can be calculated separately for bulk and boundary, as will be explained in the next section.

3.5 Phase Transitions

There are several ways to classify phase transitions. The most commonly used is the Landau classification, which is based on the principle that in a phase transition a symmetry of the system is broken [57]. The order parameter classifying the symmetry can then either make a jump, making the phase transition discontinuous as in figure 3.1b, or change smoothly, making the phase transition continuous as in figure 3.1a. An intuitive example of this is the transition from a non-magnetic to a magnetic system in the

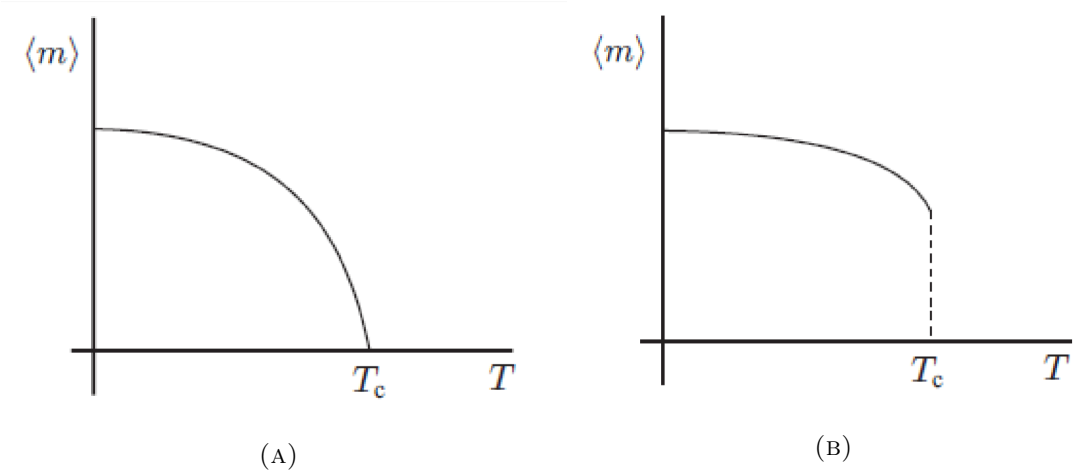

FIGURE 3.1: (A) a continuous phase transition where the order parameter (for example average magnetization) changes continuously with temperature. (B) a discontinuous phase transition, the order parameter makes a jump. Image source: [36]

Heisenberg model. In a non-magnetic system, the electron spins point in random directions and the average magnetization is zero. However, as the system is cooled down, the magnetization changes, and at zero temperature the magnetization will be maximal, all spins will point in the same direction. In this case the symmetry between up and down spin is broken, the electron spins are either up or down. We can imagine the average magnetization changing in two ways. It can change from zero smoothly to its maximal value, or it can make a jump at some point. In the Landau classification, this classifies all possible types of phase transitions. Although the Landau classification was long considered an universal method, topological phase transitions do not fit in this picture, as no underlying symmetry of the system is broken, and no local order parameter is present. Therefore, an older classification system, the Ehrenfest classification, becomes relevant.

In the Ehrenfest classification schedule, phase transitions are categorized based on the order of the derivative of the free energy with respect to the relevant thermodynamic variable that is discontinuous [58], as shown in figure 3.2. Here, no symmetry breaking is necessary to define a phase transition. Although this classification is just like the Landau classification incomplete, as it does not include transitions where the free energy or a derivative diverges, it is ideally suited to classify topological phase transitions. In reference [55] it was shown that since phase transitions are visible as discontinuities in (the derivatives of) the grand potential, separating the bulk and boundary contributions to the grand potential as explained in the previous section, makes it possible to calculate where topological phase transitions are and what their order is, separately for bulk and boundary. This is especially relevant since it has been shown in reference [9] that topological phase transitions display unexpected universalities in the order of their

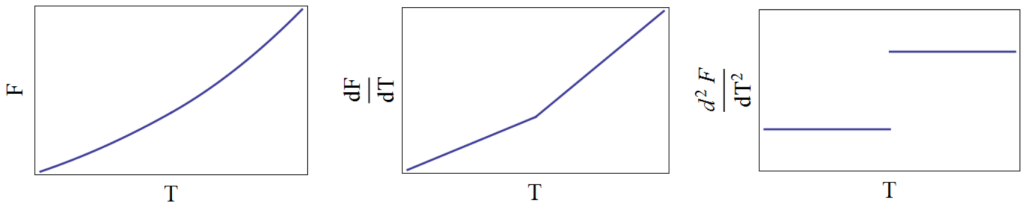

FIGURE 3.2: Ehrenfest classification. Here, we see a temperature driven phase transition where the second derivative of the free energy with respect to the temperature is discontinuous, thus the transition is second order according to the Ehrenfest classification.

phase transition. The order of the topological phase transition in bulk and boundary was calculated for several models, revealing that the order was related to the dimensionality D of the model; the edge phase transitions were all of order D and the bulk phase transitions were all of order $D + 1$. In the next chapter, we will show that this phenomenon can be understood in the framework of critical exponents.

Critical Exponents

Critical exponents are exponents that describe the behavior of various physical quantities near a phase transition. As we will see in the following section, critical exponents are quite general, they only depend on a couple of features of the system. We will first consider classical phase transitions and the role of critical exponents in this case. In the next section, we will show that these concepts can easily be translated to quantum phase transitions, in which there are no thermal fluctuations.

4.1 Classical Phase Transitions

As discussed is the previous chapter classical phase transitions can be divided in first- and higher-order transitions. In the case of first-order transitions, the first derivative of the free energy is discontinuous, and a phase transition occurs trough a coexistence of the two phases. A higher order phase transition is continuous in the first derivative of the free energy, but discontinuous in a higher order derivative. For a higher order phase transition, there is no phase coexistence, instead, there is a critical point at which one phase changes into another [59]. Near this critical point, the correlation length ξ, which is the characteristic length of a correlated region, or in other words, determines how fast the correlation between two points vanishes with increasing distance between them, diverges with exponent ν:

$$\xi \propto |t|^{-\nu} . \tag{4.1}$$

Here, t is dimensionless measure of distance from critical point. In case of a temperature driven phase transition, t would be equal to the reduced temperature $t = |T - T_c| / T_c$, where T_c is the temperature at the critical point. Analogous to the divergence in correlation length, the correlation time τ_c, which determines how fast the correlation between two points vanishes with increasing time, diverges with a different exponent νz,

$$\tau_c \propto \xi^z \propto |t|^{-\nu z} . \tag{4.2}$$

Near the critical point, the only relevant length scale is the correlation length. Thus, if we rescale all lengths in the system by a common factor b, and at the same time adjust the external parameters such that the correlation length stays the same, the physical properties of the system have to be unchanged. Thus, for the free energy f, depending

on t and some other external parameter h, we have the homogeneity relation,

$$f(t,h) = b^{-d} f(tb^{y_t}, hb^{y_h}). \tag{4.3}$$

Here y_t, y_h are critical exponents and d is the dimensionality of the system. We can now reduce the amount of independent variables by fixing $tb^{y_t} = 1$:

$$f(t,h) = t^{d/y_t} \tilde{f}(h/t^{y_h/y_t}). \tag{4.4}$$

Thus, for zero h, we have that the second derivative of f with respect to t goes as

$$|t|^{d/y_t - 2} = |t|^{-\alpha}, \tag{4.5}$$

where α is a standard critical exponent. Since the correlation length changes (like all lengths) as $\xi \to b\xi$ under a rescaling, t changes as $t \to tb^{y_t}$ with a rescaling, and $t \propto \xi^{-1/\nu}$, we have that,

$$\nu = \frac{1}{y_t}. \tag{4.6}$$

Combining equation (4.5) and (4.6) we find the Josephson hyper-scaling relation [59, 60],

$$2 - \alpha = \nu d. \tag{4.7}$$

Since $2 - \alpha$ determines the order of the phase transition, it is thus possible to predict the order of a classical phase transition, solely based on the dimension of the system and the value of the critical exponent ν.

4.1.1 Alternative Expression

In order to determine the critical exponents, it is sometimes useful to rewrite equation (4.1) and (4.2) in a different way. Since the gap size ω has the dimension of inverse time, we have $\omega \propto 1/\tau_c$. Similarly, the inverse length dimension of momentum k gives $k \propto 1/\xi$. Combining this with equation (4.2) we find that near the critical point

$$\omega \propto k^z. \tag{4.8}$$

Again writing $k \propto 1/\xi$ and using equation (4.1) this scaling relation leads to [61],

$$\omega(k = 0) \propto |t|^{\nu z}. \tag{4.9}$$

4.2 Quantum Phase Transitions

In the zero temperature limit, there are no thermal fluctuations and the phase transition is dominated by quantum fluctuations. In order to gain a deeper understanding of the difference between these zero temperature quantum phase transitions and classical phase transitions, we look at the canonical density operator e^{-H/k_BT}. This operator looks exactly like the time evolution operator in imaginary time τ, with the identification $1/k_BT = \tau = -i\Theta/\hbar$ where Θ is the real time. Therefore, it is convenient to introduce an imaginary time direction in the system, as was done in equation (2.28) and (2.29) using the path integral formalism. At zero temperature, the imaginary time direction is similar to an additional space dimension, since the extension in this direction then becomes infinite. According to equation (4.2), time scales like the length to the power z. The classical homogeneity relation of equation (4.3) can thus be rewritten for the zero temperature case as,

$$f(t,h) = b^{-(d+z)} f(tb^{y_t}, hb^{y_h}). \tag{4.10}$$

Thus we see that a quantum phase transition in d space dimensions is related to a classical phase transition in $d+z$ space dimensions [59, 62]. This results in the Josephson hyper-scaling relation for quantum phase transitions:

$$2 - \alpha = \nu(d+z). \tag{4.11}$$

Looking back to the results on the order of topological phase transitions from reference [9], introduced in the previous chapter, where the order of the topological phase transition of a D dimensional system was found to be $D+1$ in the bulk and D on the boundary, we see that this behavior is indeed accurately described by equation 4.11, in case $\nu = z = 1$. For the models studied in reference [9] this is indeed the case. However for the model by Baruselli et al. [16] this is not the case, resulting in a derivation from the universal law proposed in reference [9], as will be discussed in the next chapter.

Results

In this thesis, we use the minimal model proposed by Baruselli et al. [16], where we include all hybridization terms, up to second nearest neighbor. We will first present our solutions to the mean field equations as a function of both temperature and hybridization, which we will need for the calculation of the heat capacity and topological phase transition respectively. Then, we will present the bulk and boundary contributions to the heat capacity. Finally, we will discus the resulting phase transitions and phase diagram.

5.1 Solution to the Mean-Field Equations

The solutions to the mean-field equations were calculated iteratively using a momentum space grid. In each step of the iteration the values of λ, μ and b were adapted accordingly with respect to the iterative equations,

$$\lambda_{n+1} = \frac{1}{b_n N_s}\left(\sum_k \mathrm{Tr}\left[\left\langle f_k^\dagger c_k \right\rangle(\lambda_n,\mu_n,b_n)V_k\right] + b_n \sum_k \mathrm{Tr}\left[\left\langle f_k^\dagger f_k \right\rangle(\lambda_n,\mu_n,b_n)t_k\right]\right), \tag{5.1}$$

$$\mu_{n+1} = \mu\ \epsilon\ \mathbb{R}\ \text{s.t.}\ \left(\frac{1}{N_s}\sum_{k,\alpha}\left\langle f_{k\alpha}^\dagger f_{k\alpha}\right\rangle(\lambda_{n+1},\mu,b_n) + \frac{1}{N_s}\sum_{k,l,\sigma}\left\langle c_{k\sigma}^{(l)\dagger} c_{k\sigma}^{(l)}\right\rangle(\lambda_{n+1},\mu,b_n) - 4\right) = 0, \tag{5.2}$$

$$b_{n+1} = \sqrt{1 - \frac{1}{N_s}\sum_{k,\alpha}\left\langle f_{k\alpha}^\dagger f_{k\alpha}\right\rangle(\lambda_{n+1},\mu_{n+1},b_n)}, \tag{5.3}$$

that were derived from the mean-field equations of section 2.3.1.2. For most values of temperature and hybridization equation (5.2) was solved numerically using the standard Mathematica function ArgMin. However, in some cases of low temperature and high hybridization this was not possible with the required precision, due to both numerical and phenomenological limitations.

The phenomenological reason is that at zero temperature, the only information the μ equation gives is that the Fermi level solution should be in the gap, resulting in numerical solutions randomly placed in the gap. For low but non-zero temperature this is in principle not the case. However, there are numerical limitations when the

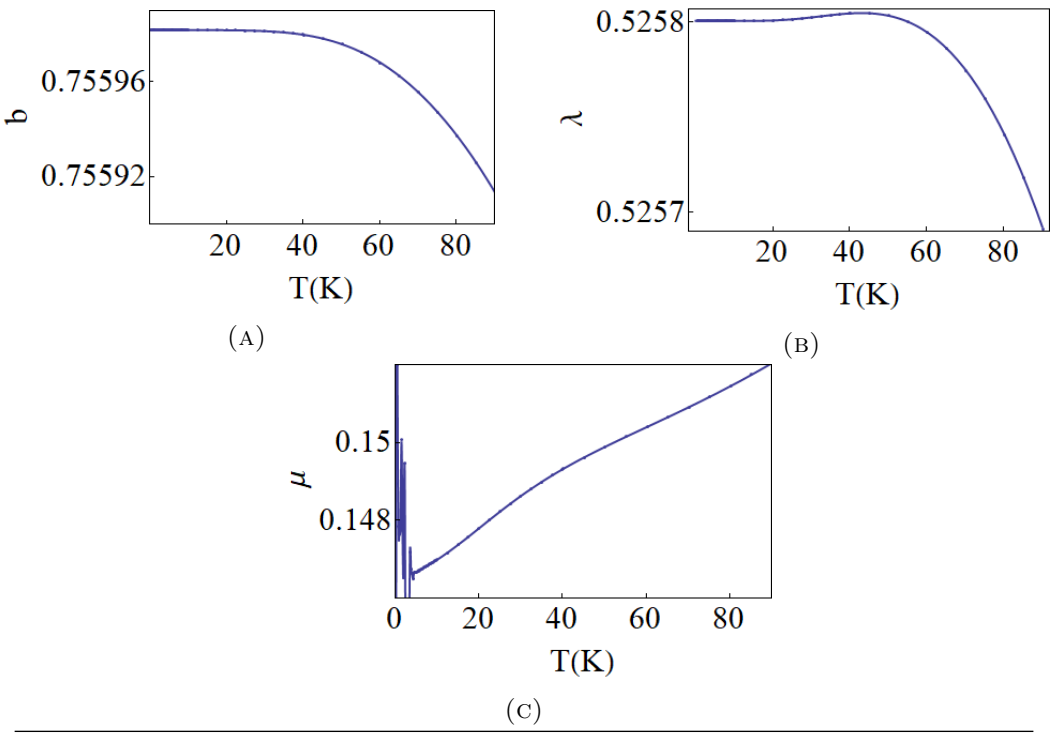

FIGURE 5.1: Solutions to the mean-field equations as a function of temperature. The solutions were obtained with a k-space grid of 15^3 points.

temperature is close enough to the $T = 0$ limit, as the results become independent for changes in μ up to machine precision.

Although the numerical limits can be extended by the use of a denser momentum space grids, this also significantly lengthens the computation time of the solving algorithm, putting a boundary on the extension of these limits.

5.1.1 As a Function of Temperature

The numerical solutions to the mean-field equations as a function of temperature using a k-space grid of 15^3 points are shown in figure 5.1. Here the hybridization of SmB_6 ($v = 0.1$) is used. We see that the solution for μ becomes unstable for low temperatures. Furthermore, we observe that the mean field parameters change minimally with a change of temperature.

5.1.2 As a Function of Hybridization

The numerical solutions to the mean-field equations as a function of hybridization using a k-space grid of 5^3 points are shown in figure 5.2 for several temperatures. Here, we see that the μ solution indeed becomes instable for low temperatures and high hybridization.

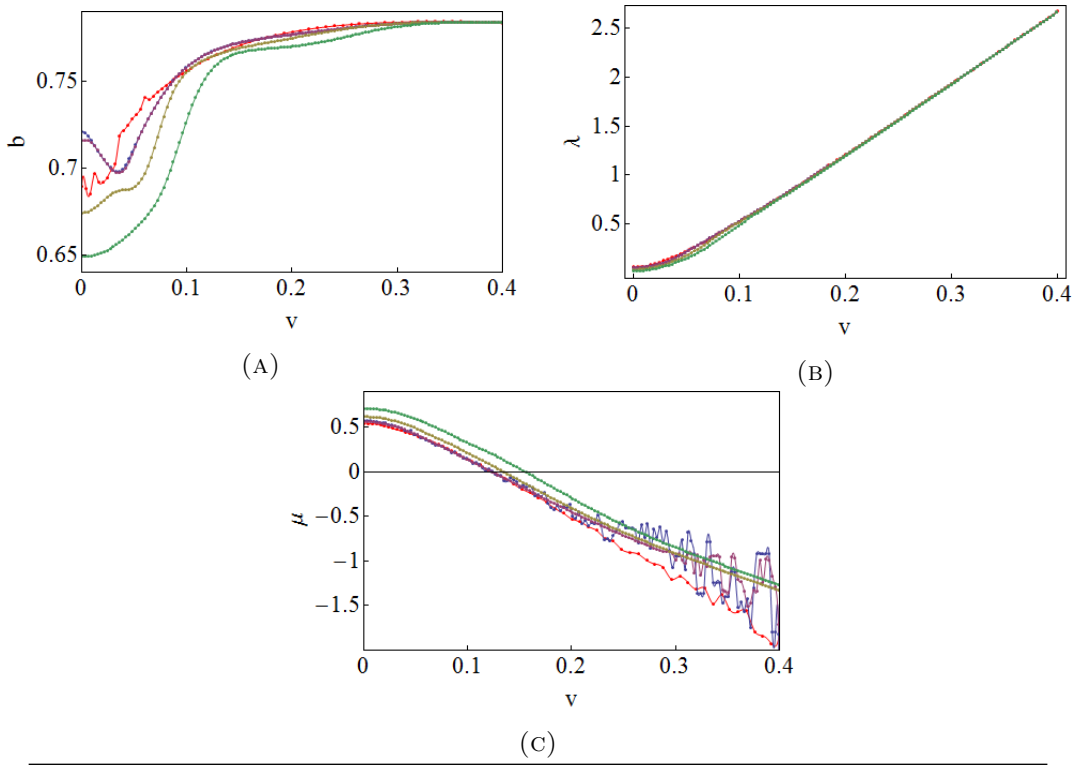

FIGURE 5.2: Solutions to the mean-field equations for different temperatures and varying hybridization strength v. Blue, pink, yellow and green indicate a temperature of 0, 100, 500, 1000 Kelvin respectively. The solutions were obtained by using a k-space grid of 5^3 points. Red indicates the solution for 0 Kelvin with a k-space grid of 13^3 points.

We also show the solution to the mean field equations for zero temperature, using a momentum grid of 15*15*400 points. Here we see that in this case, the solution for the chemical potential indeed becomes more stable.

5.2 Heat Capacity

In order to calculate the heat capacity, stable mean-field solutions as a function of temperature are necessary. Therefore, we approximated the mean-field solutions to be constant for temperatures up to 10 Kelvin. This approximation is supported by the minimal change in b and λ at temperatures below 10 Kelvin and the realization that for low temperatures with respect to the gap size, the value of μ is not important for the filling, as long as it is in the gap. This approximation led to the heat capacity shown in figure 5.3. It is important to note here, that if we convert the units of the calculated heat capacity to the units used in figure 1.1, the results are of the same order of magnitude. For the calculation of the bulk and boundary contribution to the heat capacity a system of 40 to 44 layers with a periodic k-space grid of 15^2 points was used. We see that the bulk contribution is falling of faster then linear with decreasing temperature, as we

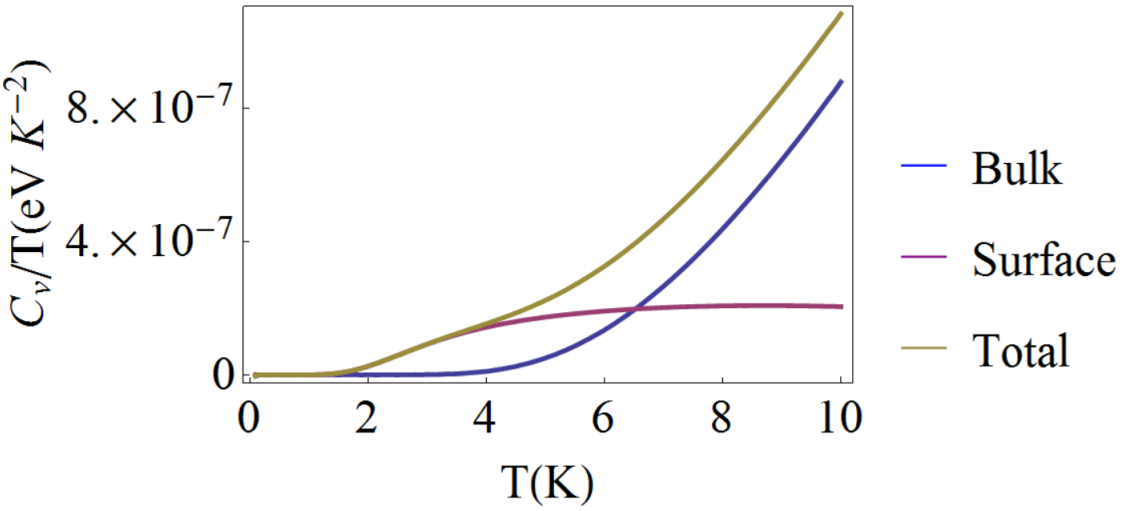

FIGURE 5.3: Heat capacity of SmB_6 for low temperatures, split in a bulk and surface contribution, and the sum of the two giving the total, for a system of 200 layers.

would expect since the bulk is insulating. On the edges however, we see the same kind of behavior, which is unexpected since the edges are metallic. This is probably due to a limited density in the periodic k-space grid.

5.3 Phase Transitions

We see three different phases in the model as the hybridization is varied from 0 to 0.4. At low hybridization there is a metallic phase, at intermediate hybridization there is a topological phase and at high hybridization there is a trivial band insulator phase. We will discuss each of the transitions separately.

5.3.1 Topological Insulator to Metal

As the hybridization decreases, there is a point where the hybridization is no longer strong enough to open up the hybridization gap, resulting in a closing of the band gap, and the system becoming metallic. As shown in figure 5.4, the band gap does not close by a touching of the bands, but closes indirectly instead.

5.3.2 Topological Insulator to Band Insulator

At zero temperature, the system undergoes a quantum phase transition at a hybridization strength of about 0.36eV. At this point, λ becomes large enough, such that the

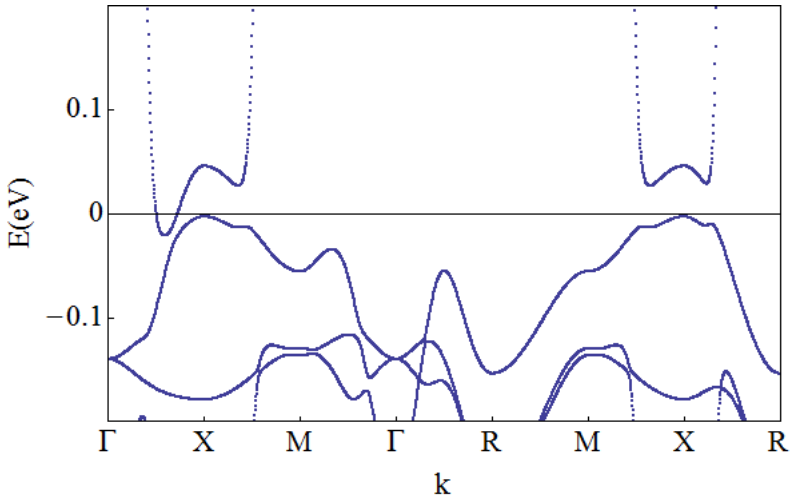

FIGURE 5.4: Indirect closing of the band gap. Here we see that as the hybridization decreases to 0.05 the band gap closes indirectly. For this figure, the mean field solutions b=0.70, λ=0.21 and μ=0.42 obtained for T=1K and a momentum space grid of 5^3 points were used.

d- and f-bands no longer overlap, and the topological invariant becomes trivial. Thus, there exists a phase transition from a topological insulator for lower v to an insulator at higher v. The resulting band structures around the phase transition are shown in figure 5.5. Here, it is indeed visible that the lowest d band is shifted over the highest f band, making only the f bands occupied at the high symmetry points, which results in a change of the topological index.

Around this phase transition, the grand potential contribution from both surface and boundary was calculated using Hill thermodynamics as described in section 3.4. Although the solutions to the mean-field equation become more stable with increasing density of the momentum space grid, we were unable to get a solution that was stable enough to see a phase transition from the grand potential within the available computation time. This problem was solved near the band insulator to topological insulator transition by making a linear approximation of μ that is in the gap, as shown in figure 5.6. For the calculation of the grand potential, the mean field equations were solved on a momentum space grid of 5^3 points with a spacing $\delta v = 0.00025$. After making a linear approximation for μ that is in the gap, as explained above, these solutions were used to calculate the grand potential of a system with a periodic k-space grid of 15^2 points and 400 to 404 layers. The resulting volume contribution is shown in figure 5.7. Here, we see a discontinuity in the third derivative, indicating a third order phase transition. The surface contribution is shown in figure 5.8, here we see a second order phase transition.

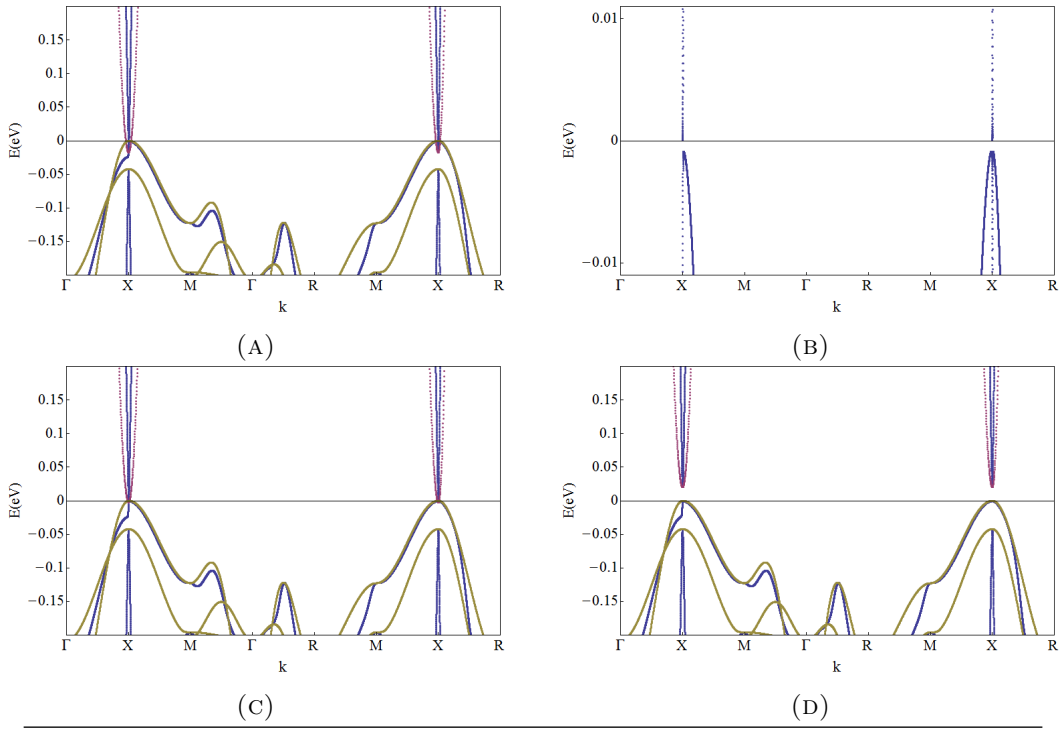

FIGURE 5.5: Band structure for different hybridization strengths. Pink and yellow indicate the un-hybridized d- and f-electrons respectively, and blue indicates the hybridized band structure. In (A) the band structure just before the phase transition is shown at $v = 0.358$ eV. (B) is a zoom of (A) where the band gap is visible. (C) depicts the band structure very close to the phase transition, at $v = 0.363$. (D) depicts the band structure after the topological phase transition at $v = 0.365$, the lowest d band here lies above the f bands, giving a trivial topological index.

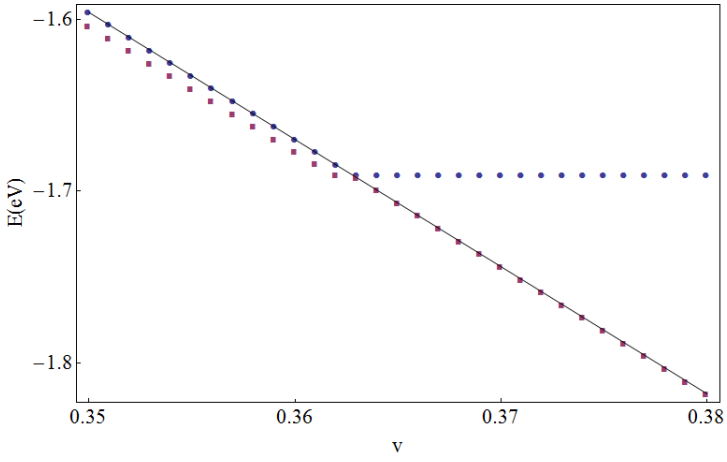

FIGURE 5.6: μ solution of the mean field equations around the topological insulator to band insulator phase transition. The blue and pink dots indicate the upper and lower bound of the gap respectively. The black line is a possible linear approximation of μ that is within the gap.

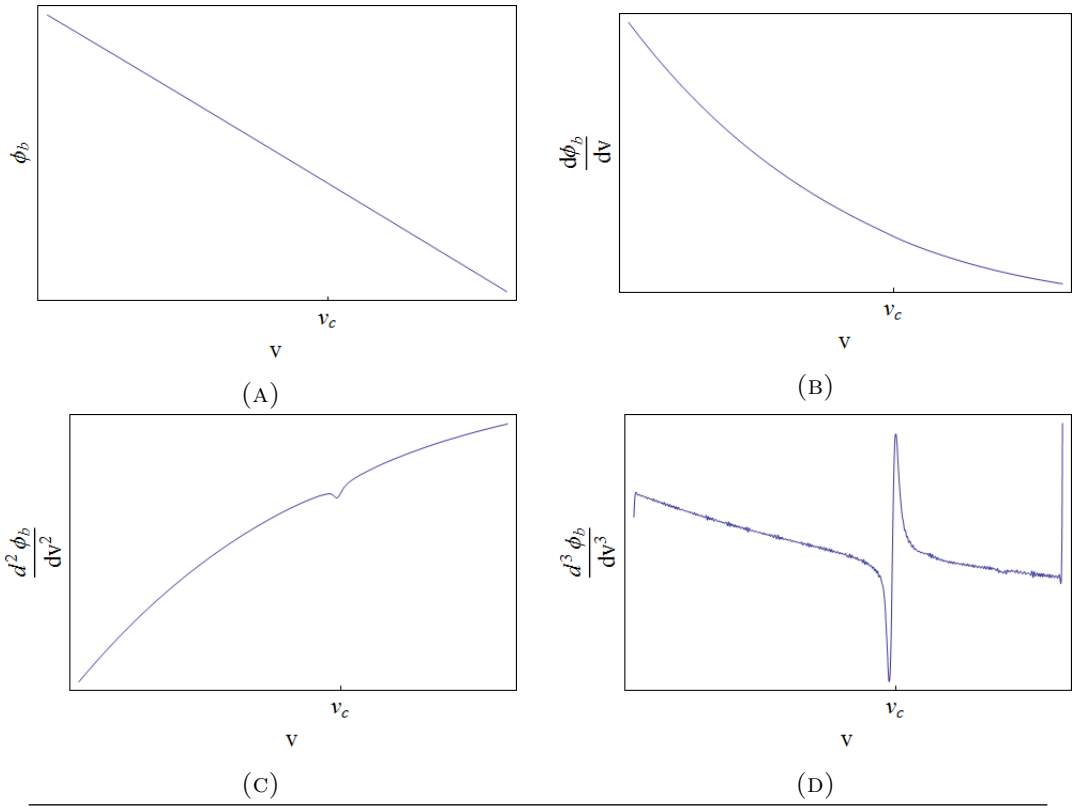

FIGURE 5.7: Bulk contribution to the grand potential ϕ_b as a function of hybridization v, and its derivatives. The third order derivative is discontinuous, indicating a third order phase transition. Note; in these calculations the sign of the parameter $\eta x 7 v 2$ from reference [16] was switched, Although this might have caused slight numerical deviations, the change does not alter the band structure significantly, and we do not expect any qualitative differences.

5.3.2.1 Critical Exponents

As explained in chapter 4, the order of the phase transition can be predicted by using the critical exponents ν and z. Using equation (4.8) and (4.9), these critical exponents were calculated by determining the gap size for different k and t as shown in figure (5.9a) and (5.9b). The resulting critical exponents are $z = 2$ and $\nu = 1/2$. Using the hyper-scaling relation of equation 4.7 we find,

$$2 - \alpha = \frac{1}{2}(d + 2)\,. \tag{5.4}$$

Thus we find $2 - \alpha = 2.5$ in the bulk and $2 - \alpha = 2$ at the boundary. This is consistent with the third order bulk, and second order boundary phase transition we find using Hill thermodynamics.

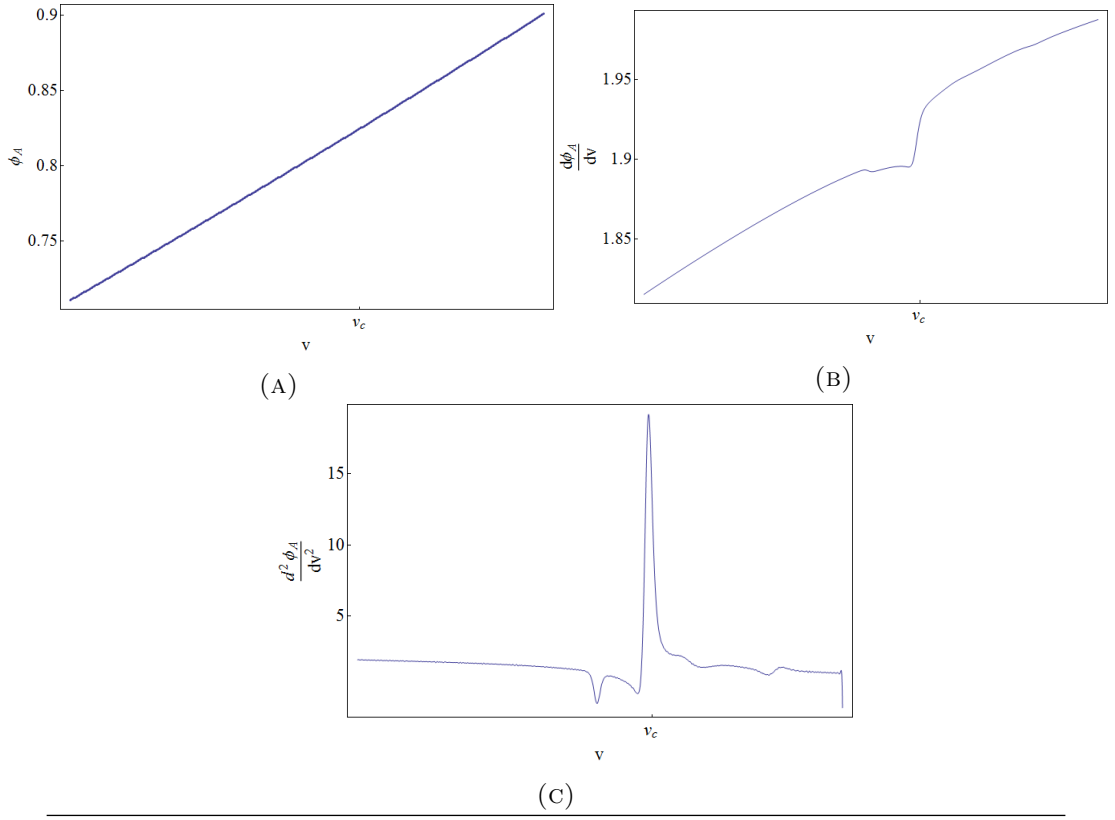

FIGURE 5.8: Surface contribution to the grand potential ϕ_A as a function of hybridization v, and its derivatives. The second order derivative is discontinuous, indicating a second order phase transition. Note; in these calculations the sign of the parameter $\eta x7v2$ from reference [16] was switched, Although this might have caused slight numerical deviations, the change does not alter the band structure significantly, and we do not expect any qualitative differences.

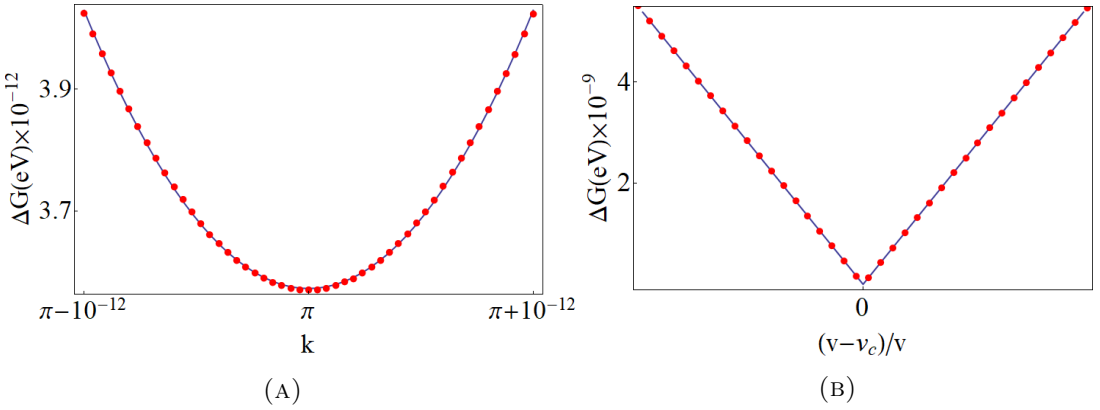

FIGURE 5.9: Gap size as a function of (A) k at the critical point and (B) hybridization at $k = 0$. The dots indicate the calculated gap size. In (A) a quadratic fit to the date is plotted. Using equations (4.8) and (4.9) we find $\nu z = 1$ and $z = 2$. The mean-field solutions used for these figures were obtained for zero temperature on a momentum space grid of 5^3 points.

5.3.3 Phase Diagram

Having identified the different phases of the model, we can now calculate the phase diagram by solving the mean-field equations for different temperatures and calculating the hybridization for which the gap closes at these temperatures. These gap closings then give the phase transition, since the phases can only change as the gap closes. The results are shown in figure 5.10. Here we see that the boundary between the phases barely changes with increasing temperature. We note that for SmB_6, which has a hybridization $v = 0.1$, there is no temperature driven phase transition at temperatures for which the model is valid. This absence could be since the Anderson lattice model is not valid above the Kondo temperature, and the mean-field approximation is only valid for low temperatures.

To calculate the transition points in figure 5.10 a momentum space grid of 5^3 points was used to solve the mean-field equations, for the metal to topological Kondo insulator transition the mean field equations were solved with $\delta v = 0.003$, and for the topological Kondo insulator to band insulator transition the mean field equations were solved with $\delta v = 0.0003$, in between the points, an interpolation function was used.

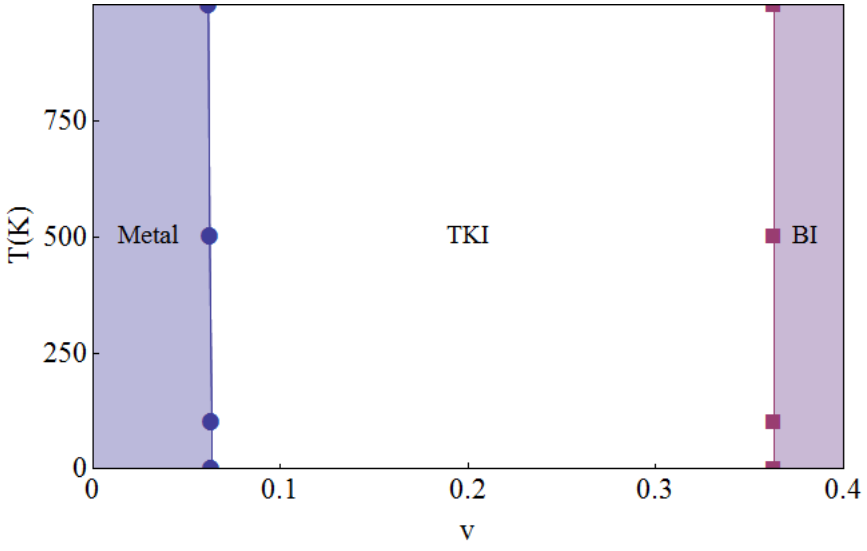

FIGURE 5.10: Phase diagram of SmB_6 modeled by the model proposed by Baruselli et al. [16]. We see a metal phase with no gap, a topological Kondo insulator (TKI) phase with a gap and non trivial topological invariant, and a band insulator phase with a gap and trivial topological invariant.

Discussion and Conclusion

In this thesis, we investigated thermodynamics of the proposed topological Kondo insulator SmB_6, using a mean-field slave boson approximation and Hill thermodynamics. In particular, we considered the order of the topological Kondo insulator to band insulator phase transition, and the bulk and boundary contribution of the system to the heat capacity. We found that the order of the phase transition can be accurately predicted using critical exponents of the system, namely a third ordered one in the bulk and a second ordered one on the surface. Furthermore, we found that the anomalous behavior of the heat capacity of SmB_6 in experiments can probably not be explained by the edges in a mean-field model.

By obtaining these results we used several approximations. The most obvious approximation is the slave-boson mean-field approximation. However, the starting Hamiltonian, the Anderson lattice model is already a mean-field approximation that is only valid at low temperatures. The validity of our results for finite temperatures are therefore questionable, as is inherent to mean-field theory. Additionally, it was shown in reference [63] that the introduction of interactions to a system can change the order of a phase transition, and even give a first order topological phase transition. Furthermore, as discussed previously, in reference [10], it was shown that the low temperature bulk heat capacity can significantly change when excitons are considered. Therefore, it is interesting to further investigate the influence of interactions on the topological phase transition in the model used in this thesis.

Within the mean-field theory, several other approximations were made. It was assumed that the mean-field parameters were constant through out the system, which as shown by [64], does not have to be true for finite-size systems. Furthermore, the mean field equations were solved on a periodic k-space grid. As shown in figure 5.2 the density of the k-space grid influences the mean-field solutions. However, in the region of the topological phase transition this influence is much less pronounced. In order to decrease the effect of these approximations, even denser k-space grids can be used, and the mean-field parameters can be allowed to vary with the distance to the edge. This would, however significantly increase the computation time required to find solutions to the mean-field equations. Finally, in the calculation of the grand potential, the bulk and boundary contribution were estimated by making a linear fit. For this method to be correct, the system needs to be large enough to prevent interaction between the boundaries. In order to make the results more reliable, bigger system sizes can be used. However, since we have checked that there is a close resemblance between the results obtained from the

finite system for the bulk and the results for the infinite model, it is unlikely that this will have much effect on the results.

The calculated heat capacity from figure 5.3 does not reproduce the experimentally measured upturn in figure 1.1. Although this might be caused by a limited momentum space grid that does not detect the edge states properly, recent theoretical results by Knolle et al. [10] indicate that the upturn is indeed not a surface but instead a bulk effect. The effect of the boundary on the heat capacity of a SmB_6 sample is currently experimentally investigated by J. P. Paglione, unfortunately the results of this research are not yet available. We conclude that the edge states are probably not responsible for the upturn in the heat capacity. However, a calculation with a bigger k-space grid is necessary to fully investigate the influence of the edge states on the heat capacity in the used mean-field model.

The phase diagram calculated from the mean field solutions in the previous chapter differs significantly from the phase diagram previously calculated by Dzero et al. [11]. The most notable difference is that as the hybridization goes to zero, we do not find the transition to a $b = 0$ solution that is described in reference [11]. Even if we solve the mean field equations for the model used by Dzero et al., we can not detect this transition. We therefore conclude that the origin of the difference is in the solving algorithm for the mean-field equations. After contact with the authors and detailed comparison of the algorithms used, we found two main differences. First of all, the definitions of the mean-field equations are slightly different. Where we used a finite k-space grid, Dzero et al. numerically integrated over continuous k. Although this could explain the difference, one would then expect our solutions to converge to the solutions by Dzero et al. for increasing density of k points. However, as we increased the k space density up to 25^3 points, no such convergence was found. Secondly, the solving algorithm used is different. Where we used an iterative method where one solution generates the next one through a rewriting of the mean field equations, Dzero et al. used a derivative based solving algorithm, a modification of the Powell hybrid method. This difference in method could explain the difference in result, if one of the methods finds a local stable point instead of the global solution. Although we found a high sensitivity of the method by Dzero et al. to starting conditions, which to supports the idea of a local minimum, it also seems oddly coincidental that a local minimum would give such (besides the $b = 0$ behavior) similar solutions. Therefore, further investigation of this problem is necessary.

Unfortunately, since for SmB_6 the hybridization v is equal to 0.1, it is far away from the phase transitions in the phase diagram of figure 5.10. This makes it extremely difficult to experimentally study the topological phase transition. This is supported by experimental measurements of the phase diagram of SmB_6 with varying temperature

and pressure in reference [65]. Here, we see that although the pressure can influence the hybridization [66], there is no pressure induced band insulator to topological Kondo insulator phase transition. Therefore, it would be interesting to investigate the possibility of other materials being closer to this phase transition, since the material might cross the phase boundary by either tuning the temperature, crossing the phase boundary in figure 5.10 vertically, or by indirectly tuning the hybridization of the system and crossing the phase boundary horizontally. Unfortunately, the hybridization can not be tuned as a single parameter. It is, however, influenced by external parameters like the pressure, as mentioned before, and magnetization [66]. This motivates further research on the influence of these parameters on the model. Additionally it would be interesting to see how the model responds to the presence of bulk carbon content, as it has been experimentally shown in reference [7] that this can systematically increase the surface conductivity of SmB_6.

Another interesting topic for further research would be to see if the topological phase transition, and its order, can also be calculated using correlation functions. The idea behind this is that correlation functions, similar to the grand potential, display a discontinuity (in the derivative) with respect to the relevant thermodynamic parameter. This might also provide a natural way to include interactions, as they can be incorporated through first loop corrections to the correlation functions.

Bibliography

[1] David Hsieh, Dong Qian, Lewis Wray, YuQi Xia, Yew San Hor, Robert Joseph Cava, and M Zahid Hasan. A topological dirac insulator in a quantum spin hall phase. *Nature*, 452(7190):970–974, 2008.

[2] N Xu, X Shi, PK Biswas, CE Matt, RS Dhaka, Y Huang, NC Plumb, M Radović, JH Dil, E Pomjakushina, et al. Surface and bulk electronic structure of the strongly correlated system smb_6 and implications for a topological kondo insulator. *Physical Review B*, 88(12):121102, 2013.

[3] A Menth, E Buehler, and TH Geballe. Magnetic and semiconducting properties of smb_6. *Physical Review Letters*, 22(7):295, 1969.

[4] JW Allen, B Batlogg, and P Wachter. Large low-temperature hall effect and resistivity in mixed-valent sm b 6. *Physical Review B*, 20(12):4807, 1979.

[5] Maxim Dzero, Kai Sun, Victor Galitski, and Piers Coleman. Topological kondo insulators. *Physical review letters*, 104(10):106408, 2010.

[6] Nan Xu, Hong Ding, and Ming Shi. Spin-and angle-resolved photoemission on the topological kondo insulator candidate: Smb_6. *Journal of Physics: Condensed Matter*, 28(36):363001, 2016.

[7] WA Phelan, SM Koohpayeh, P Cottingham, JW Freeland, JC Leiner, CL Broholm, and TM McQueen. Correlation between bulk thermodynamic measurements and the low-temperature-resistance plateau in smb_6. *Physical Review X*, 4(3):031012, 2014.

[8] JC Nickerson, RM White, KN Lee, Robert Bachmann, TH Geballe, and GW Hull Jr. Physical properties of sm b 6. *Physical Review B*, 3(6):2030, 1971.

[9] SN Kempkes, A Quelle, and C Morais Smith. Universalities of thermodynamic signatures in topological phases. *Scientific Reports*, 6, 2016.

[10] Johannes Knolle and Nigel R Cooper. Excitons in topological kondo insulators: Theory of thermodynamic and transport anomalies in smb_6. *Physical Review Letters*, 118(9):096604, 2017.

[11] MO Dzero. Symplectic large-n theory of topological heavy-fermion semiconductors. *The European Physical Journal B*, 85(9):1–8, 2012.

[12] Jan Werner and Fakher F Assaad. Interaction-driven transition between topological states in a kondo insulator. *Physical Review B*, 88(3):035113, 2013.

[13] JH Pixley, Rong Yu, Silke Paschen, and Qimiao Si. Global phase diagram and momentum distribution of single-particle excitations in kondo insulators. *arXiv preprint arXiv:1509.02907*, 2015.

[14] Terrell L Hill. *Thermodynamics of small systems*. Courier Corporation, 1963.

[15] Maxim Dzero, Kai Sun, Piers Coleman, and Victor Galitski. Theory of topological kondo insulators. *Physical Review B*, 85(4):045130, 2012.

[16] Pier Paolo Baruselli and Matthias Vojta. Scanning tunneling spectroscopy and surface quasiparticle interference in models for the strongly correlated topological insulators smb_6 and pub_6. *Physical Review B*, 90(20):201106, 2014.

[17] https://upload.wikimedia.org/wikipedia/commons/0/0b/Band_gap_comparison.svg.

[18] Philip W Anderson. Absence of diffusion in certain random lattices. *Physical review*, 109(5):1492, 1958.

[19] M Zahid Hasan and Charles L Kane. Colloquium: topological insulators. *Reviews of Modern Physics*, 82(4):3045, 2010.

[20] John Bardeen, Leon N Cooper, and John Robert Schrieffer. Theory of superconductivity. *Physical Review*, 108(5):1175, 1957.

[21] Vincent Mourik, Kun Zuo, Sergey M Frolov, SR Plissard, EPAM Bakkers, and LP Kouwenhoven. Signatures of majorana fermions in hybrid superconductor-semiconductor nanowire devices. *Science*, 336(6084):1003–1007, 2012.

[22] A Yu Kitaev. Unpaired majorana fermions in quantum wires. *Physics-Uspekhi*, 44 (10S):131, 2001.

[23] Marcel Franz. Majorana's wires. *Nature nanotechnology*, 8(3):149–152, 2013.

[24] MV Berry. Classical adiabatic angles and quantal adiabatic phase. *Journal of Physics A: Mathematical and General*, 18(1):15, 1985.

[25] Maxim Dzero, Jing Xia, Victor Galitski, and Piers Coleman. Topological kondo insulators. *arXiv preprint arXiv:1506.05635*, 2015.

[26] János Asbóth, László Oroszlány, and András Pályi. Topological insulators. *http://fizipedia.bme.hu/images/1/14/Topological_insulators.pdf*, page 46, 2013.

[27] Liang Fu and Charles L Kane. Topological insulators with inversion symmetry. *Physical Review B*, 76(4):045302, 2007.

[28] B Andrei Bernevig and Taylor L Hughes. *Topological insulators and topological superconductors*. Princeton University Press, 2013.

[29] Alexander Altland and Martin R Zirnbauer. Nonstandard symmetry classes in mesoscopic normal-superconducting hybrid structures. *Physical Review B*, 55(2): 1142, 1997.

[30] Andreas P Schnyder, Shinsei Ryu, Akira Furusaki, and Andreas WW Ludwig. Classification of topological insulators and superconductors in three spatial dimensions. *Physical Review B*, 78(19):195125, 2008.

[31] Alexei Kitaev, Vladimir Lebedev, and Mikhail Feigelman. Periodic table for topological insulators and superconductors. In *AIP Conference Proceedings*, volume 1134, pages 22–30. AIP, 2009.

[32] Andreas P Schnyder, Shinsei Ryu, Akira Furusaki, Andreas WW Ludwig, Vladimir Lebedev, and Mikhail Feigelman. Classification of topological insulators and superconductors. In *AIP Conference Proceedings*, volume 1134, pages 10–21. AIP, 2009.

[33] Shinsei Ryu, Andreas P Schnyder, Akira Furusaki, and Andreas WW Ludwig. Topological insulators and superconductors: tenfold way and dimensional hierarchy. *New Journal of Physics*, 12(6):065010, 2010.

[34] Peter S Riseborough. Heavy fermion semiconductors. *Advances in Physics*, 49(3): 257–320, 2000.

[35] Alexander Cyril Hewson. *The Kondo problem to heavy fermions*, volume 2. Cambridge university press, 1997.

[36] Henk TC Stoof, Koos B Gubbels, and Dennis BM Dickerscheid. *Ultracold quantum fields*, volume 1. Springer, 2009.

[37] Tetsuya Takimoto. Smb_6: A promising candidate for a topological insulator. *Journal of the Physical Society of Japan*, 80(12):123710, 2011.

[38] Feng Lu, JianZhou Zhao, Hongming Weng, Zhong Fang, and Xi Dai. Correlated topological insulators with mixed valence. *Physical review letters*, 110(9):096401, 2013.

[39] Dae-Jeong Kim, J Xia, and Z Fisk. Topological surface state in the kondo insulator samarium hexaboride. *Nature materials*, 13(5):466–470, 2014.

[40] Steven Wolgast, Çağlıyan Kurdak, Kai Sun, JW Allen, Dae-Jeong Kim, and Zachary Fisk. Low-temperature surface conduction in the kondo insulator smb_6. *Physical Review B*, 88(18):180405, 2013.

[41] Xiaohang Zhang, NP Butch, P Syers, S Ziemak, Richard L Greene, and Johnpierre Paglione. Hybridization, inter-ion correlation, and surface states in the kondo insulator smb_6. *Physical Review X*, 3(1):011011, 2013.

[42] Madhab Neupane, Nasser Alidoust, SuYang Xu, Takeshi Kondo, Yukiaki Ishida, Dae-Jeong Kim, Chang Liu, Ilya Belopolski, YJ Jo, Tay-Rong Chang, et al. Surface electronic structure of the topological kondo-insulator candidate correlated electron system smb_6. *Nature communications*, 4, 2013.

[43] Juan Jiang, Sheng Li, Tong Zhang, Zhe Sun, Fei Chen, ZR Ye, Min Xu, QQ Ge, SY Tan, XH Niu, et al. Observation of possible topological in-gap surface states in the kondo insulator smb_6 by photoemission. *Nature communications*, 4, 2013.

[44] Chul-Hee Min, P Lutz, S Fiedler, BY Kang, BK Cho, H-D Kim, H Bentmann, and F Reinert. Importance of charge fluctuations for the topological phase in smb_6. *Physical review letters*, 112(22):226402, 2014.

[45] Jonathan D Denlinger, James W Allen, Jeong-Soo Kang, Kai Sun, Byung-II Min, Dae-Jeong Kim, and Zachary Fisk. Smb_6 photoemission: past and present. In *Proceedings of the International Conference on Strongly Correlated Electron Systems (SCES2013)*, page 017038, 2014.

[46] Emmanouil Frantzeskakis, Nick de Jong, Berend Zwartsenberg, YK Huang, Yu Pan, Xin Zhang, JX Zhang, FX Zhang, LH Bao, Ojiyed Tegus, et al. Kondo hybridization and the origin of metallic states at the (001) surface of smb_6. *Physical Review X*, 3 (4):041024, 2013.

[47] Z-H Zhu, A Nicolaou, G Levy, NP Butch, P Syers, XF Wang, J Paglione, GA Sawatzky, IS Elfimov, and A Damascelli. Polarity-driven surface metallicity in smb_6. *Physical review letters*, 111(21):216402, 2013.

[48] Nan Xu, PK Biswas, RS Dhaka, G Landolt, S Muff, CE Matt, X Shi, NC Plumb, M Radovic, E Pomjakushina, et al. Direct observation of the spin texture in strongly

correlated smb_6 as evidence of the topological kondo insulator. *arXiv preprint arXiv:1407.8118*, 2014.

[49] P Hlawenka, K Siemensmeyer, E Weschke, A Varykhalov, J Sánchez-Barriga, NY Shitsevalova, AV Dukhnenko, VB Filipov, S Gabáni, K Flachbart, et al. Samarium hexaboride: A trivial surface conductor. *arXiv preprint arXiv:1502.01542*, 2015.

[50] Michael M Yee, Yang He, Anjan Soumyanarayanan, Dae-Jeong Kim, Zachary Fisk, and Jennifer E Hoffman. Imaging the kondo insulating gap on smb_6. *arXiv preprint arXiv:1308.1085*, 2013.

[51] Wei Ruan, Cun Ye, Minghua Guo, Fei Chen, Xianhui Chen, Guang-Ming Zhang, and Yayu Wang. Emergence of a coherent in-gap state in the smb_6 kondo insulator revealed by scanning tunneling spectroscopy. *Phys. Rev. Lett.*, 112:136401, Mar 2014. doi: 10.1103/PhysRevLett.112.136401. URL http://link.aps.org/doi/10.1103/PhysRevLett.112.136401.

[52] Sahana Rößler, Tae-Hwan Jang, Dae-Jeong Kim, LH Tjeng, Zachary Fisk, Frank Steglich, and Steffen Wirth. Hybridization gap and fano resonance in smb_6. *Proceedings of the National Academy of Sciences*, 111(13):4798–4802, 2014.

[53] Victor Alexandrov, Maxim Dzero, and Piers Coleman. Cubic topological kondo insulators. *Physical review letters*, 111(22):226403, 2013.

[54] Xiaoyu Deng, Kristjan Haule, and Gabriel Kotliar. Plutonium hexaboride is a correlated topological insulator. *Physical review letters*, 111(17):176404, 2013.

[55] Anton Quelle, Emilio Cobanera, and C Morais Smith. Thermodynamic signatures of edge states in topological insulators. *Physical Review B*, 94(7):075133, 2016.

[56] Josiah Willard Gibbs. On the equilibrium of heterogeneous substances. *American Journal of Science*, (96):441–458, 1878.

[57] E Lifeshitz and L Landau. *Statistical physics*. The Charendon Press, Oxford, 1938.

[58] Stephen J Blundell and Katherine M Blundell. *Concepts in thermal physics*. OUP Oxford, 2009.

[59] Matthias Vojta. Quantum phase transitions. *Reports on Progress in Physics*, 66 (12):2069, 2003.

[60] Alexander Altland and Ben D Simons. *Condensed matter field theory*. Cambridge University Press, 2010.

[61] Mucio A Continentino. Quantum scaling in many-body systems. 2001.

[62] Mucio A Continentino. Quantum scaling in many-body systems. *Physics reports*, 239(3):179–213, 1994.

[63] A Amaricci, JC Budich, M Capone, B Trauzettel, and G Sangiovanni. First-order character and observable signatures of topological quantum phase transitions. *Physical review letters*, 114(18):185701, 2015.

[64] Pier Paolo Baruselli and Matthias Vojta. Kondo holes in topological kondo insulators: Spectral properties and surface quasiparticle interference. *Physical Review B*, 89(20):205105, 2014.

[65] Yazhou Zhou, Qi Wu, Priscila FS Rosa, Rong Yu, Jing Guo, Wei Yi, Shan Zhang, Zhe Wang, Honghong Wang, Shu Cai, et al. Quantum phase transition and destruction of kondo effect in pressurized smb_6. *arXiv preprint arXiv:1603.05607*, 2016.

[66] Qimiao Si and Silke Paschen. Quantum phase transitions in heavy fermion metals and kondo insulators. *physica status solidi (b)*, 250(3):425–438, 2013.